Quantitative Relationships between Basalt Geochemistry, Shear Wave Velocity and Asthenospheric Temperature Beneath Western North America

Quantitative Relationships between Basalt Geochemistry, Shear Wave Velocity and Asthenospheric Temperature Beneath Western North America

M. Klöcking[1], N. J. White[1], J. Maclennan[1], D. M^{c}Kenzie[1], J. G. Fitton[2]

[1]Bullard Laboratories, Department of Earth Sciences, University of Cambridge, Madingley Rise, Madingley Road, Cambridge, CB3 0EZ, UK

[2]School of GeoSciences, University of Edinburgh, Grant Institute, The King's Buildings, James Hutton Road, Edinburgh, EH9 3FE, UK

Key Points:

- Correlation between basalt geochemistry and shear wave velocities
- Mantle potential temperatures of 1340 ± 20 °C
- Uplift and magmatism generated by modest thermal anomalies beneath thinned plate

Corresponding author: M. Klöcking, N.J. White, mk618@cam.ac.uk, njw10@cam.ac.uk

Abstract

Western North America has an average elevation that is ∼2 km higher than cratonic North America. This difference coincides with a westward decrease in average lithospheric thickness from ∼240 km to <100 km. Tomographic models show that slow shear wave velocity anomalies lie beneath this region, coinciding with the pattern of basaltic magmatism. To investigate relationships between magmatism, shear wave velocity and temperature, we analyzed a suite of >260 basaltic samples. Forward and inverse modeling of carefully selected major, trace and rare earth elements were used to determine melt fraction as a function of depth. Basaltic melt appears to have been generated by adiabatic decompression of dry peridotite with asthenospheric potential temperatures of 1340 ± 20 °C. Potential temperatures as high as 1365 °C were obtained for the Snake River Plain. For the youngest (i.e. <5 Ma) basalts with a subplate geochemical signature, there is a positive correlation between shear wave velocities and trace element ratios such as La/Yb. The significance of this correlation is explored by converting shear wave velocity into temperature using a global empirical parameterization. Calculated temperatures agree with those determined by inverse modeling of rare earth elements. We propose that regional epeirogenic uplift of western North America is principally maintained by widespread asthenospheric temperature anomalies lying beneath a lithospheric plate, which is considerably thinner than it was in Late Cretaceous times. Our proposal accounts for the distribution and composition of basaltic magmatism and is consistent with regional heatflow anomalies.

Plain Language Summary

Marine fossils from western North America show that this region, which includes the states of Arizona, Colorado and Utah, was below sea level 80 million years. Since that time, large-scale uplift of about 2 kilometers has occurred. This uplift coincides with massive outpourings of lava, the youngest of which occurred 1000 years ago at Sunset Crater outside Flagstaff and was witnessed by Native Americans. Seismic (i.e. acoustic) images of the deep structure beneath western North America show that the tectonic plate is only about 50 to 100 kilometers thick— much thinner than beneath the Great Plains further east. Here, we use chemical analyses of different lavas to calculate the temperature of mantle rocks that lie beneath the tectonic plate and which generated the lavas. Remarkably, this temperature is consistent with the temperature that is estimated from the speed of sound through these mantle rocks. We con-

clude that the whole of Western North America is supported by a combination of moderately warm mantle rocks and a thinner than expected tectonic plate.

1 Introduction

It is recognized that convective circulation of the Earth's mantle generates and maintains some fraction of surface topography, referred to as dynamic topography [*Anderson et al.*, 1973; *Parsons and Daly*, 1983; *Hager and Richards*, 1989; *Lithgow-Bertelloni and Silver*, 1998; *Moucha et al.*, 2008; *Flament et al.*, 2013]. A significant corollary is that the spatial and temporal evolution of dynamic topography can help to constrain the behavior of mantle convection on geologic timescales. Western North America constitutes a dramatic example where large-scale regional uplift appears to be supported by sub-plate processes [*Ashwal and Burke*, 1989]. Remnants of extensive marine deposits, such as the Mancos shale of the Mesaverde Group that crops out across Wyoming, Utah and Colorado, demonstrate that a Mid-Cretaceous seaway originally connected the Beaufort Sea and the Gulf of Mexico [*Roberts and Kirschbaum*, 1995]. This observation implies that present-day regional elevation principally grew during Cenozoic times. Thermochronologic observations from the Grand Canyon area combined with clumped isotopic studies of Paleogene lacustrine deposits suggest that this elevation grew in several discrete stages [e.g. $\sim$70 and $\sim$30 Ma; *Moucha et al.*, 2009; *Liu and Gurnis*, 2010]. This inference is supported by inverse modeling of drainage networks and by the history of sedimentary flux into basins, such as the Gulf of Mexico [*Galloway et al.*, 2011; *Roberts et al.*, 2012].

A region encompassing the Basin and Range Province, the Snake River Plain and the Colorado Plateau sits $\sim$2 km higher than cratonic North America (Figure 1a). Crustal thickness of the Colorado Plateau is $\sim$45 km, which is similar to that of the Great Plains [*Shen and Ritzwoller*, 2016]. Given that their respective crustal velocities and inferred densities are similar, this difference in elevation cannot easily be explained by crustal isostasy [e.g. *Sheehan et al.*, 1995; *Spencer*, 1996; *Shen and Ritzwoller*, 2016]. Instead, regional elevation of western North America is probably supported either by a thinner lithosphere, by convective upwelling of anomalously hot asthenospheric mantle, or by some combination of both mechanisms [e.g. *Bradshaw et al.*, 1993; *Hyndman and Currie*, 2011; *Becker et al.*, 2013; *Afonso et al.*, 2016]. Surface wave tomographic models show that beneath most of western North America the continental lithosphere is less than 120 km thick, whereas beneath the interior craton the lithosphere is about 240 km thick [*Priestley and M^{c}Kenzie*, 2013]. Receiver function analyses suggest that a thin lithosphere underlies western North America since Sp conversions have

been reported at depths of 60–80 km [*Lekić and Fischer*, 2014; *Hopper et al.*, 2018]. The reason for such a large difference in lithosperic thickness across the continent remains obscure. It has been proposed that mechanical thinning of the lithosphere is somehow linked to shallow subduction of the Farallon slab [*Humphreys*, 1995; *Spencer*, 1996]. More speculatively, delamination of lithospheric mantle following slab hydration has been invoked [*Humphreys et al.*, 2003]. A long wavelength (i.e. 500–4000 km) positive free-air gravity anomaly of +40 mGal is centered on the Yellowstone area [Figure 1b; *Bruinsma et al.*, 2014]. This cruciform anomaly reaches across most of western North America, coinciding with the distribution of Cenozoic magmatism and with the planform of a regional heatflow anomaly [*Pollack et al.*, 1993].

Tomographic models show that there are large negative shear wave velocity anomalies beneath most of western North America at depths of 50–500 km [Figure 1c; e.g. *Crow et al.*, 2010; *Schmandt and Humphreys*, 2010; *Obrebski et al.*, 2011; *Shen et al.*, 2013; *Burdick et al.*, 2014; *Schaeffer and Lebedev*, 2014; *Shen and Ritzwoller*, 2016]. Different models disagree on the detailed horizontal and vertical structure of these anomalies and on the amplitudes of phase velocity measurements, but the general pattern is both consistent and striking. The slowest velocity anomalies occur beneath the Yellowstone area, consistent with a protruding finger of hot material that extends along the Snake River Plain towards cratonic lithosphere located further east. A similarly slow finger lies beneath the Rio Grande Rift and a horseshoe-shaped anomaly fringes the Colorado Plateau. In conjunction with positive free-air gravity anomalies, these regional velocity anomalies are consistent with the presence of a shallow convective upwelling beneath the North American plate.

Magmatism of western North America is spatially distributed over a region that broadly coincides with elevated regional topography. Volcanism reaches far into the continental plate and reveals age progressions that can largely be accounted for by horizontal plate translation over a relatively stationary source of melting within the asthenospheric mantle. Basaltic volcanism commenced at ∼80 Ma and its subsequent temporal evolution has several distinct phases, the most significant of which are a dramatic increase in the volume of magmatism at ∼40 Ma and a marked switch from a lithospheric to an asthenospheric signature at ∼5 Ma [*Fitton et al.*, 1991; *Kempton et al.*, 1991]. The spatial distribution of Neogene basaltic volcanism closely coincides with the pattern of shear wave velocity anomalies (Figure 1c).

Two classes of models have been proposed to account for these large-scale observations. One school of thought invokes an upwelling mantle plume located beneath present-day Yellowstone with secondary plumes triggering volcanism further south [e.g. *Leat et al.*, 1991; *Parsons et al.*, 1994; *Saltus and Thompson*, 1995; *Camp and Hanan*, 2008; *Hanan et al.*, 2008; *Moucha et al.*, 2009; *Pierce and Morgan*, 2009; *Huang et al.*, 2015]. An alternative view is that mantle material flows off the edge of cratonic lithosphere and around complex remnants of the sinking Farallon slab, triggering shallower convective upwelling [e.g. *Roy et al.*, 2009; *van Wijk et al.*, 2010; *James et al.*, 2011; *Levander et al.*, 2011; *Levander and Miller*, 2012; *Refayee et al.*, 2013; *Ballmer et al.*, 2015]. The principal difference between these plume and flow models centers on the temperature of the underlying asthenospheric mantle. In a plume model, mantle material is expected to be hotter than in flow models where convection could be edge-driven or generated by shallow return flow of mantle material. In this contribution, our principal aim is to shed some light on these different hypotheses by calculating depths and temperatures of mantle melting beneath western North America from the geochemistry of mafic igneous rocks. A significant part of our strategy is to combine a quantitative geochemical approach with the results of shear wave tomographic studies. By integrating geochemical and geophysical observations, we hope to illuminate aspects of upper mantle processes that may have influenced the spatial and temporal evolution of western North America.

2 Basaltic Magmatism

In order to isolate the source of intracontinental volcanism, it is important to identify and remove crustal and/or mantle lithospheric contamination so that we can focus attention on the most primitive (i.e. asthenospheric) melts that contain information about initial melting conditions. Many contributions highlight the bimodal nature of potential source compositions beneath western North American basalts. For example, Hf and Nd isotopes from some basalts of the Western Transition Zone that fringes the Colorado Plateau, and from the Colorado Plateau itself, suggest some overlap with the oceanic mantle array. The isotopic composition of other samples from the same volcanic fields is also consistent with the presence of components of Paleoproterozoic peridotitic lithosphere [*Reid et al.*, 2012]. Given our aims, we are principally concerned with basaltic rocks that are as compositionally similar to ocean island basalts (OIBs) as possible. It is therefore appropriate to filter out contributions from metasomatized lithospheric mantle, or from subduction-influenced magmatism, where hydrous melting and contamination with sedimentary material can be significant.

2.1 Sample Selection and Screening

We have assembled a substantial and comprehensive database of Cenozoic mafic igneous rocks. This database comprises >1000 analyses from the western North American volcanic and intrusive rock catalogue (NAVDAT; `http://www.navdat.org`), 215 samples collected by *Fitton et al.* [1991], 29 samples from the Western Transition Zone generously provided by T. Plank [written communication, 2015; *Plank and Forsyth*, 2016], as well as 65 samples collected across Arizona and Colorado during December 2014 and April 2015, respectively. The geographic distribution of all analyses and samples is summarized in Figure 2. Samples collected in the field and those selected from the catalogue of *Fitton et al.* [1991] were analyzed for trace and rare earth elements (REEs) using inductively coupled plasma-mass spectrometry (ICP-MS). The 65 samples collected from Arizona and Colorado were analyzed for major and trace elements using X-ray fluorescence (XRF). Based on their respective precisions, XRF measurements of V, Y, Zr, Nb, Cr, Cu, Sc, Ni, Sr and Zn together with ICP-MS measurements of Ba, REEs, Rb, Th and Pb were used for further study. Detailed analytical procedures and data tables are provided in Supplementary Information.

The combined database is sub-divided into ten geographic provinces shown in Figure 2: Snake River Plain (SRP), Great Plains (GP), Eastern Transition Zone (ETZ), Southern Transition Zone (STZ), Sentinel Plain (SE), Northern Basin and Range (NBR), Western Transition Zone (WTZ), Basin and Range (BR), Rio Grande Rift (RGR), and Colorado Plateau (CP). Samples from the Cascades and from the western Great Basin were excluded due to their proximity to the present-day subduction zone. Compositions of remaining samples range from basaltic andesite to picrobasalt and basanite. The majority of these samples fall within the basaltic field. Samples from the Colorado Plateau are the most enriched in terms of alkaline and incompatible elements, while samples from the Snake River Plain have the most depleted signatures. Major and trace element contents were used to identify the most primitive, least fractionated rocks from each province. A cut-off of MgO $\geq$7 wt% was deemed appropriate in order to minimize the effects of pyroxene and plagioclase fractionation (Figure 3). For provinces with large numbers of high MgO samples, it was feasible to adopt a more severe (i.e. more primitive) cut-off value. For example, samples with MgO $\geq$8 wt% were selected from the Snake River Plain and from the Southern Transition Zone.

Rigorous screening is used to exclude samples that are obviously contaminated by interaction with lithospheric melts. Trace element composition was used to identify samples de-

rived from the asthenosphere, following an approach similar to that described by *Fitton et al.* [1991]. Thus, samples were deemed to be of asthenospheric origin if their La, Ba and Nb compositions fall within the fields expected for global suites of mid-ocean ridge basalts (MORB) and/or of OIBs [Figure 3d; *Stracke et al.*, 2005; *Willbold and Stracke*, 2006]. Partition coefficients show that these particular elements are highly incompatible in olivine and remain within the liquid phase [i.e. $D_{La} = D_{Nb} = 5{\times}10^{-4}$, $D_{Ba} = 5{\times}10^{-6}$; *Salters and Stracke*, 2004]. Their relative abundances are largely insensitive to fractionation processes and, instead, are broadly reflective of source composition and of melting conditions. Arc magmas are typically enriched in large ion lithophiles, such as Ba, and depleted in Nb relative to MORB or OIB. In contrast, OIB, MORB and subduction zone melts have similar concentrations of La for a given melt fraction [e.g. *Pearce*, 1982]. Consequently, screening on the basis of La/Ba and La/Nb ratios helps to identify the chemical influence of subducting slabs (Figure 3c). It is possible, however, that volatile-rich fluids that are not produced by a slab could pass this form of screening. Where available, Sr and Nd isotope ratios were used to check the efficacy of the screening process for identifying only MORB- or OIB-type compositions.

This screening strategy reduces the combined database to 177 acceptable samples: 12 out of 272 for Snake River Plain; 8 out of 76 for Great Plains; 13 out of 32 for the Eastern Transition Zone; 18 out of 42 for the Southern Transition Zone; 5 out of 9 for Sentinel Plain; 2 out of 11 for Northern Basin and Range; 40 out of 102 for Western Transition Zone; 7 out of 28 for Basin and Range; 65 out of 150 for Rio Grande Rift; and 7 out of 14 for Colorado Plateau. 77 of the total number of the chosen samples and analyses are taken from *White et al.* [2004], *Thompson et al.* [2005], *Leeman et al.* [2009] and *Plank and Forsyth* [2016]. A total of 100 samples were extracted and analyzed from the catalogue of *Fitton et al.* [1991] and from the inventory collected during the two field campaigns. Two of these samples duplicate those of *Leeman et al.* [2009] and so the average composition was used. The majority of these samples are younger than 5 Ma [*Fitton et al.*, 1991]. Trace element values for the screened database are summarized in Figure 4.

2.2 Melting Model and its Application

Relative abundances of incompatible elements can be used to determine primary melting conditions provided that a series of assumptions are made about the nature of the source region and about the process of melt extraction. Here, trace elements from the screened database, notably the REEs, are used to determine the degree of mantle melting as a function of depth.

As a result of their differences in compatibility (i.e. partitioning behavior between solid and liquid phases), REEs are sensitive to the cumulative amount of melting and to the relative proportions of melting that occur within the garnet and spinel stability fields. The cumulative volume of generated melt is strongly influenced by the temperature at the time of melting. Higher temperatures give rise to a larger solidus overstep and so produce larger melt fractions [*McKenzie and Bickle*, 1988]. Ratios of light REEs to medium or heavy REEs, such as La/Sm or La/Yb, are negatively correlated with melt fraction due to different degrees of incompatibility of these elements. The partition coefficients of La, Sm and Yb in the mantle at 2 GPa are 6.6×10^{-3}, 6×10^{-2} and 1.15×10^{-1}, respectively [*Salters and Stracke*, 2004]. The smaller the melt fraction, the larger the differences in behavior of the relatively more compatible Sm and Yb with respect to the more incompatible La. Hence, large values of La/Sm and La/Yb are associated with small melt fractions. Depth of melting is determined relative to the stability fields of spinel and garnet. For example, large ratios of Sm/Yb indicate melting of garnet peridotite since a greater proportion of Yb is retained within garnet of the solid phase and does not partition into the melt phase.

The exact depth of the spinel-garnet transition is a subject of ongoing debate. Until recently, it was thought that this transition was highly sensitive to temperature such that the greater the temperature, the deeper and narrower the transition zone should be. A conservative estimate of this temperature sensitivity is 40 ± 10 °C/kbar [*Klemme and O'Neill*, 2000; *Walter et al.*, 2002]. However, *Green et al.* [2012] and *Jennings and Holland* [2015] argue that the pressure of the garnet-spinel transition was overestimated in previous experimental studies, largely due to the simplicity of the phase systems used (i.e. Mg-Al-Si rather than Ca-Mg-Al-Si). *Jennings and Holland* [2015] demonstrate that their model compares well to existing studies, provided that simplifying corrections are applied, notably allowing for Ca activity within garnet. In their thermodynamic calculations, the depth and thickness of the transition zone at, or above, the solidus is not especially sensitive to temperature. Instead, a variation of up to 5 kbar toward lower pressures for a temperature range of 880–1300 °C is found. By contrast, increasing concentrations of Cr and Fe^{3+} within peridotite tend both to increase the thickness of the transition and to cause a shift to greater pressures due to the greater stability of spinel [*Klemme and O'Neill*, 2000; *Jennings and Holland*, 2015]. For the KLB-1 peridotite, *Jennings and Holland* [2015] calculate the pressure at the top and bottom of the spinel-garnet transition where it intersects the solidus and obtain values of 21.4 and 21.7 kbar, respectively.

An inverse modeling strategy enables REE compositions to be fitted by varying melt fraction as a function of depth for a specified source composition. Here, we apply the INVMEL-v12.0 algorithm, the first version of which was originally described by *M^{c}Kenzie and O'Nions* [1991]. This approach is especially sensitive to the relative amount of melting that occurs within the garnet and spinel stability fields. Distributions of REE compositions are matched by assuming isentropic decompression melting of a dry aluminous peridotite mantle source. For a given inverse model, the depth to the top of the melting region, the depth interval, and an initial distribution of melt fraction as a function of depth can be specified. An optimal fit is obtained by iteratively computing the point-and-depth average composition using a continuous melting curve. The root mean squared (rms) misfit between observed and calculated REE distributions is minimized using a conjugate direction search routine called Powell's algorithm [*Press et al.*, 1992]. When the optimal melt fraction as a function of depth is determined, the composition of other trace and major elements can be predicted by forward modeling. In general, melting interval and total melt fraction are the most reliable outputs of this inverse modeling approach. The calculated melt fraction distribution is compared with a set of predicted isentropic curves to estimate the potential temperature of melting, where potential temperature is calculated at the Earth's surface using an adiabatic gradient of 0.48 °C km^{-1}. These curves are determined for different potential temperatures using a decompression melting model with a dry solidus parameterization described by *Katz et al.* [2003]. For our purposes, an entropy of melting, $J = 400$ J K^{-1} kg^{-1}, is used in order to be self-consistent [*Kojitani and Akaogi*, 1997]. If calculated melt fraction distributions deviate from an isentropic path, a range of potential temperatures is gauged from the deepest and shallowest melt fractions.

The INVMEL algorithm exploits partition coefficients calculated using the lattice strain model of *Blundy and Wood* [2003]. We assume that the pressures at the top and the bottom of the spinel-garnet transition are 21 and 24 kbar, which correspond to depths of 63 and 72 km, respectively. This transition zone is thicker than that proposed by *Jennings and Holland* [2015] in order to stabilize the inverse algorithm— a difference that does not materially affect our results. The combination of a different solidus parameterization together with different depth and thickness of the spinel-garnet transition zone compared with *M^{c}Kenzie and O'Nions* [1991] means that temperature estimates at any given depth are generally 30–50 °C lower. Thus whilst cumulative melt fractions are generally comparable, our results yield minimum estimates of both temperature and lithospheric thickness.

We assume that asthenospheric mantle can be regarded, to a first approximation, as homogeneous beneath western North America. Modeling is generally carried out using a mixture of primitive and depleted MORB mantle. Source composition is gauged using ε_{Nd} values of samples from each volcanic field published in the NAVDAT catalogue. For example, if $\varepsilon_{Nd} = 10$ a depleted mantle source is used and if $\varepsilon_{Nd} = 0$ a primitive mantle source is used [*White and M^{c}Kenzie*, 1995]. An important exception is the Colorado Plateau which is characterized by high concentrations of the most incompatible elements that cannot easily be fitted by inverse modeling. Additional enrichment of the source region by adding a small fraction of melt generated within the garnet stability field was required to optimize the fit between observed and calculated concentrations. Published isotopic measurements and mantle sources used for inverse modeling are summarized in Table 1. Compositions of depleted and primitive mantle, as well as the small fraction of melt generated within the garnet stability field are provided in the Supplementary Information.

Judicious sample selection is an important prerequisite since only near-fractional melting of a uniform dry peridotite source is accounted for during inverse modeling. Once samples have been selected, amounts of olivine fractionation are determined using the differences between observed MgO and FeO concentrations and those calculated for a primitive melt of the specified source composition [*M^{c}Kenzie and O'Nions*, 1991]. In this way, the final melt fraction distribution is appropriately corrected. This approach also holds, within limits, for clinopyroxene fractionation. However, it cannot be used to correct for the crystallisation of non-Mg/Fe bearing phases such as plagioclase, which is the reason why sample selection is so important. No corrections are applied for contamination by crust and/or lithospheric mantle (i.e. melting is assumed to be generated from a homogeneous asthenospheric source). The effect of volatiles, or of a non-peridotitic source composition, on melting beneath western North America is separately addressed. This general strategy is used to determine the depth and degree of melting beneath 26 volcanic fields from ten geographic provinces. Average major, trace and rare earth element compositions for these provinces are provided in Table 1.

2.3 Results

Inverse models for each province are shown in Figures 5 and 6 and summarized in Table 2. The observed REE concentrations are fitted such that the rms misfit between observed and calculated ratios with respect to the source is < 0.9. Forward-modeled fits to other trace element concentrations are largely within the degree of uncertainty for geochemical compo-

sitions with minor exceptions (Figures 5 and 6b,e,h,m,p). For all provinces, more compatible elements are better matched than highly incompatible ones. We stress that only fractionation of olivine has been formally corrected for and so hydrous phases (e.g. amphibole, phlogopite) that are observed in basalts from the Hopi Buttes volcanic field of the Colorado Plateau could account for depletion of Na, Rb, P and K.

Cumulative melt fraction and depth of melting systematically vary across western North America. Volcanic fields from the Snake River Plain represent the largest degrees of melting ($\sim$10 %) at the shallowest melting depths ($\sim$50 km), corresponding to the highest potential temperatures for this region ($\sim$1365 °C). In contrast, basalts from the Colorado Plateau have the smallest melt fractions ($\sim$1 %) that formed at the greatest depths ($>$ 62 km), corresponding to the lowest potential temperatures ($\sim$1320 °C). These differences between Snake River Plain and Colorado Plateau basalts are significant and reflect different concentrations of light REEs relative to heavy REEs. Analyses from the Great Plains, from the Eastern and Southern Transition Zones, and from Sentinel Plain yield melt fractions of $\sim$6–7% at depths of 53–84 km, corresponding to potential temperatures of $\sim$1350–1360 °C. Analyses from the Basin and Range, from the Western Transition Zone and from the Rio Grande Rift yield 2–4 % melting at depths between 54 and 74 km, equivalent to potential temperatures of 1320–1330 °C. Degrees of olivine fractionation generally vary between 16 and 31%. Note that in all cases, most melt production occurs either within the spinel-only stability field or within the spinel-garnet transition zone.

Errors associated with these results can be gauged by considering a combination of random and systematic uncertainties [*White et al.*, 1992; *Brodie et al.*, 1994]. First, the typical standard deviation of geographically averaged sample concentrations is less that 10%, which gives rise to an uncertainty in cumulative melt fraction of less than 2%. Secondly, the top of the melting column can be adjusted in each case by $\pm$2–5 km, which contributes an uncertainty in cumulative melt fraction of less than 2%. Thirdly, the depth and thickness of the spinel-garnet transition can be varied by ± 5 km and ± 10 km, respectively. These variations yield a combined uncertainty in cumulative melt fraction of less than 3%. It is important to emphasise that more significant excursions in the values of the top of the melting column and in the depth and thickness of the transition lead to degraded fits to the observed REE concentrations. Uncertainties associated with source composition constrained by ε_{Nd} act to change the depth to the top of the melting column by < 10 km, which yields an uncertainty in cumulative melt

fraction of less than 5%. Together, these estimates of the range of uncertainties for cumulative melt fraction generate potential temperature variations of $\pm$10–30 °C.

A significant outcome of our study is that the bulk of melting beneath western North America occurred close to the garnet-spinel transition. Since this transition is fixed at a depth range of 63–72 km, significant melting is required to occur shallower than $\sim$70 km. Mafic compositions are consistent with mantle potential temperatures of 1320–1365 °C. The highest temperatures are obtained for the youngest Snake River Plain samples whilst those from the Colorado Plateau do not record potential temperatures that are significantly different to that of ambient asthenospheric mantle. Previous inverse modeling yielded potential temperatures of $\sim$1400 °C at depths of 60–100 km beneath the Snake River Plain and beneath the Rio Grande Rift [*White and M^{c}Kenzie*, 1995; *Thompson et al.*, 2005]. It has been suggested that the top of the melting region corresponds to the base of the lithospheric plate [*M^{c}Kenzie and O'Nions*, 1991; *White et al.*, 1992]. The average plate thickness inferred by inverse modeling is 55 $\pm$10 km. Beneath the Snake River Plain, melts are generated at depths as shallow as 48 km and beneath the Colorado Plateau, melts are generated at depths of $>$ 62 km. Although our results suggest that basaltic melting is generated within the asthenospheric mantle layer immediately beneath the lithospheric plate, elevated ^{3}He/^{4}He ratios from hot-spring gases on the Snake River Plain and from parts of the Basin and Range Province indicate that deeper, more primitive, mantle also plays a role [*Craig et al.*, 1978; *Kennedy et al.*, 1985; *Welhan et al.*, 1988; *Jordan*, 2002; *Kennedy and van Soest*, 2007; *Graham et al.*, 2009].

3 Earthquake Tomographic Models

Slow wave-speed anomalies have been identified at depths of greater than $\sim$50 km beneath western North America [e.g. *Crow et al.*, 2010; *Schmandt and Humphreys*, 2010; *Obrebski et al.*, 2011; *Shen et al.*, 2013; *Burdick et al.*, 2014; *Schaeffer and Lebedev*, 2014; *Shen and Ritzwoller*, 2016]. Here, we target a subset of four tomographic models which reveal the detailed structure of the shallow mantle where melts are inferred to have been generated (Figure 7). The chosen models are PM2012, SL2013NA, DNA13 and WUSA16 that were developed by *Priestley and M^{c}Kenzie* [2013], by *Schaeffer and Lebedev* [2014], by *Porritt et al.* [2014], and by *Shen and Ritzwoller* [2016], respectively. *Porritt et al.* [2014] and *Shen and Ritzwoller* [2016] exploit the USArray database for western North America. *Schaeffer and Lebedev* [2014] address the North American continent and also included USArray data. *Priestley and M^{c}Kenzie* [2013] constructed a lower resolution global model. Despite differences in the

wavelength and amplitude of velocity anomalies, these models mostly agree with respect to the gross pattern of anomalies beneath western North America. Here, we use these models to investigate the relationship between shear wave velocity, V_s, basalt geochemistry and temperature.

The region of western North America addressed by this study is similar to that discussed by *Afonso et al.* [2016] who carried out a joint inversion of the gravity field, shear wave velocity, together with major element compositions of basaltic rocks and other geophysical observables by employing a Monte Carlo scheme. This ambitious approach tends to conceal the major variations in sensitivity possessed by different types of observations. For example, *Priestley and M^{c}Kenzie* [2006] and *Schutt and Lesher* [2006] found that depletion of fertile upper mantle by removal of a basaltic melt changes shear wave velocity by less than 1%. In contrast, a reduction of $\sim$20% occurs as temperature approaches the solidus temperature. Since the functional form of $V_s(T)$ is both uncertain and controversial, the dependence of V_s on the extent of depletion can be safely ignored. Two different approaches have been used to determine $T(V_s, P)$, both of which are empirical and suffer from the lack of any detailed physical understanding of the grain boundary processes involved. *Faul and Jackson* [2007] parameterized detailed laboratory experiments. The problem with this approach is that $T(V_s)$ is strongly dependent on grain size and the mantle grain size is likely to be two orders of magnitude greater than that used in laboratory experiments. The other approach, which is exploited here, is to use geophysical estimates of $V_s(T, P)$ to determine the relevant parameters by exploiting the functional form for this relationship proposed by *McCarthy et al.* [2011]. This approach is similar to that of *Priestley and M^{c}Kenzie* [2013] with two modifications.

The first modification concerns the solidus temperature and melt fraction as a function of temperature and pressure. Here, we use the parameterization of these quantities described by *Katz et al.* [2003] to calculate the initial temperature at a spreading ridge, and the average interior potential temperature of mantle required to generate 7 km of oceanic crust. The resultant changes from the estimates of *M^{c}Kenzie and Bickle* [1988] are small. For example, the revised average potential temperature is 1326 °C (instead of 1315 °C). The second modification involves using two activation energies to describe the Maxwell viscosity, η, so that

$$\frac{1}{\eta} = \frac{1}{\eta_1} + \frac{1}{\eta_2}, \tag{1}$$

where

$$\eta_i = A_i \exp\Big[\Big(\frac{E_i + (P - P_r)V_i}{R}\Big)\Big(\frac{1}{T} - \frac{1}{T_r}\Big)\Big]. \tag{2}$$

In this equation, $A_1 = 3.846 \times 10^{21}$ Pa s, $A_2 = 4.201 \times 10^{27}$ Pa s, $E_1 = 402 \times 10^3$ kJ/mol, $E_1 = 2805 \times 10^3$ kJ mol^{-1}, $V_1 = 0$ m^3, $V_2 = 3.112 \times 10^{-5}$ m^3, $P_r = 1.5$ GPa, and $T_r = 1473$ K. R is the gas constant and T the temperature in Kelvin. The purpose of using two viscosities, where the second one has a large activation energy, is to model the rapid decrease in V_s with increasing temperature which occurs near the solidus. The unrelaxed shear modulus, μ, is given by

$$\mu = \mu_0 + \Big(\partial\mu/\partial P\Big)_T P + \Big(\partial\mu/\partial T\Big)_P T, \tag{3}$$

where $\mu_0 = 69.27$ GPa, $\Big(\partial\mu/\partial P\Big)_T = 2.679$, $\Big(\partial\mu/\partial T\Big)_P = -9.231 \times 10^{-3}$ GPa K^{-1}, and P is pressure in GPa. These expressions for V_s are affected by the presence of melt. For example, experimental studies show that the presence of melt fractions as small as 0.25% cause viscosity to decrease by about two orders of magnitude [*Faul and Jackson*, 2007; *McCarthy and Takei*, 2011]. The amount of melt that is retained within the mantle is unlikely to exceed $\sim$0.1% [*Priestley and M^{c}Kenzie*, 2006]. This assumption is corroborated by U-series disequilibrium studies at mid-oceanic ridges [*M^{c}Kenzie*, 2000]. Although the physics of melt extraction and retention is poorly understood, we have allowed for an appropriate reduction in viscosity when temperature is close to that of the dry solidus by including η_2 in the parameterization.

In this way, $T(z)$ is calculated from $V_s(z)$, which constrains the potential temperature beneath each volcanic field. We can also estimate lithospheric thickness from the $V_s(z)$ relationship using the method described by *Priestley and M^{c}Kenzie* [2006] and *Priestley and M^{c}Kenzie* [2013]. A geothermal profile is fitted to $T(z)$ and the lithospheric thickness is obtained by extrapolating the conductive portion of the geothermal profile to the depth where it intersects the adiabatic profile. Finally, we point out that the empirical parameterization used is calibrated against an updated 2016 version of the PM2012 model (`http://ds.iris.edu/ds/products/emc-cam2016`). This parameterization yields satisfactory results when applied to all of the models under consideration.

3.1 Velocity-Temperature Calibration

We extract vertical profiles of $V_s(z)$ at ten locations for each one of the four tomographic models. These locations are chosen as representative of the average velocity structure for each volcanic province (Figures 7 and 8). While there are significant differences between these velocity profiles, there are also important commonalities. In all four models, the slowest shear

wave velocities are observed beneath the Snake River Plain. The fastest velocities are observed beneath the Colorado Plateau and beneath the Great Plains. In general, V_s between 60 and 100 km is slower than that of the WUS reference model [*Pollitz*, 2008]. Notable exceptions are velocity profiles for the Colorado Plateau taken from the WUSA16 model and for both the Colorado Plateau and the Great Plains taken from the SL2013NA model. Both of these profiles are positioned close to a sharp lateral change in shear wave velocity at the edge of cratonic lithosphere, where velocities are faster than the relevant reference model. Hence, these anomalously fast V_s profiles are probably not representative of the melting region beneath Colorado Plateau and Great Plains.

Temperature profiles correspond to potential temperatures of ∼1320–1380 °C (Figure 7b,d,f,h). In accordance with the V_s profiles, the Snake River Plain is the hottest region, Colorado Plateau has ambient or only marginally elevated temperatures, and the other provinces fall in between. The smallest variability is observed for profiles from the DNA13 model, which can be attributed to damping effects (Figure 7c). The SL2013NA and WUSA16 models predict similar temperature ranges, although the specific order of provinces can differ due to small variations in the proximity to lateral velocity gradients in each case. Lithospheric thicknesses calculated from shear wave velocity profiles are less than ∼100 km for all four models. Recent (<10 Ma) volcanic activity is focused within regions where the lithosphere is 50–55 km thick (Figure 9). There is a reasonable correspondence between estimated temperatures at 75 km depth and the distribution of youthful volcanic activity. The DNA13 model is much smoother than the other models and so its range of calculated temperatures is narrower and estimated lithospheric thicknesses are probably too small.

3.2 Comparing Temperature Estimates

It is illuminating to compare seismically and geochemically determined temperatures. There is a reasonable qualitative correlation between the location and amplitude of slow V_s anomalies and the spatial distribution of basaltic volcanism (Figure 7). Comparison of V_s anomalies and geochemical compositions for the screened volcanic database suggests that the ratio of light to heavy REEs (e.g. La/Yb) correlates with shear wave velocities between depths of ∼60 and ∼100 km with an optimal correlation at a depth of ∼75 km where melting probably starts (Figure 10a,c,e,g). This ratio broadly reflects a combination of melt fraction and the depth of melting. Since the depth of melting is similar for samples in the analytical database used here (i.e. the bulk of melting occurs within the spinel field or within the spinel-garnet

transition zone), La/Yb can be regarded as a proxy for melt fraction. The highest values of La/Yb are recorded for the Colorado Plateau where the fastest values of V_s are observed. The smallest values of La/Yb are recorded for the Snake River Plain where the slowest values of V_s are observed. Considerable variation of V_s is observed within volcanic fields. One possible cause of this scatter is that much volcanic activity is concentrated at boundaries between anomalously fast and slow velocities. Inevitably, the melting process samples asthenospheric mantle at a spatial resolution that is smaller than that resolved by teleseismic observations. Lateral melt migration can cause additional uncertainties. Note that at near-solidus temperatures, V_s rapidly decreases [*Priestley and M^{c}Kenzie*, 2013]. Thus modest temperature excursions within a given province can have a significant effect on shear wave velocities.

Despite these complications, it is useful to directly compare potential temperatures determined from basalt geochemistry with those determined from coincident shear wave velocity profiles (Figure 10b,d,f,h). Temperatures calculated from basaltic geochemistry typically have uncertainties of ± 15 °C, which reflect analytical errors and geographical averaging together with systematic errors associated with the depth and thickness of the spinel-garnet transition zone. Temperatures calculated from shear wave velocities typically have uncertainties of up to ± 15 °C, which reflect geographical averaging. Uncertainties that are a consequence of the velocity-temperature calibration have not been included [*Priestley and M^{c}Kenzie*, 2013]. A reasonable correlation exists between both sets of potential temperatures with the highest pair of values occurring beneath the Snake River Plain and the lowest pair of values occurring beneath the Colorado Plateau. Differences in seismically determined temperatures from different models can be attributed to variations in spatial resolution, in damping, and in the spatial positioning of sharp lateral velocity gradients. Overall, the DNA13 model yields temperatures that lie within a narrower band compared with the other three models. We suggest that the WUSA16 model yields the optimal correlation.

4 Discussion

We infer that a combination of anomalously hot asthenosphere and lithospheric thinning has caused regional uplift of western North America during Cenozoic times. It is less obvious what role the foundering and fragmenting Farallon slab plays. Despite a wealth of geologic, geophysical and geochemical observations, there has been much debate about possible mechanisms of melt generation. For example, it is suggested that location and style of basaltic magmatism are mainly controlled by the thickness and basal topography of the lithosphere so

that sharp gradients at the base of the lithosphere trigger edge-driven convection or shear-driven upwelling [e.g. *van Wijk et al.*, 2010; *Ballmer et al.*, 2015]. It has also been suggested that magmatism is triggered by tearing of the subducting Farallon slab and/or by melting of metasomatized lithospheric drips [e.g. *Humphreys et al.*, 2003; *van Wijk et al.*, 2010; *James et al.*, 2011; *Zhou et al.*, 2018]. *Roy et al.* [2009] argue that conductive heating and thinning of the lithosphere following slab removal could produce uplift and magmatism. The principal difficulty with some of these proposals is their inability to generate both kilometer-scale regional uplift and basaltic volcanism. Here, we elaborate on four general observations that help to support our results. First, we summarize additional evidence for lithospheric thickness changes and for elevated sub-plate temperatures beneath western North America. We then test alternative schemes of generating basaltic melts. Finally, we consider the relationship between our results, regional heatflow anomalies, and the spatial and temporal pattern of regional uplift.

4.1 Lithospheric Thickness

There have been significant advances in our understanding of the crustal, lithospheric and sub-lithospheric structure beneath western North America [e.g. *Lin et al.*, 2011; *Hansen et al.*, 2013; *Hopper et al.*, 2014; *Shen and Ritzwoller*, 2016]. A striking observation is that crustal thicknesses beneath the Great Plains are similar to, or exceed, those beneath the Colorado Plateau, even though their respective elevations are $<$500 m and $>$2000 m [Figure 1; *Shen and Ritzwoller*, 2016]. This substantial elevation difference can only be maintained by crustal isostasy if crust beneath the Great Plains is 0.15 Mg/m^3 denser than crust beneath the elevated plateaux. This density difference would require crustal velocities beneath the Great Plains to be faster by $\sim$1 km/s, which is not observed [*Hansen et al.*, 2013; *Schmandt et al.*, 2015]. Thus simple isostatic constraints indicate that the topographic elevation of western North America is supported by density variations within the lithospheric and/or the sub-lithospheric mantle [*Levandowski et al.*, 2018].

Tomographic models demonstrate that the continental lithosphere beneath western North America is approximately one half of the thickness of the cratonic lithosphere beneath the Great Plains [e.g. *Priestley and M^{c}Kenzie*, 2013; *Schaeffer and Lebedev*, 2014]. These models also indicate that slow shear wave velocity anomalies exist in the upper mantle beneath western North America, although the spatial distribution of these slow anomalies is complicated by the presence of fast anomalies at depths of 300–600 km beneath the Colorado Plateau that are probably associated with the Farallon plate [*Obrebski et al.*, 2011]. Existence of continental litho-

sphere that is 50–100 km thick is corroborated to some extent by receiver function studies of the lithosphere-asthenosphere boundary [*Kumar et al.*, 2012; *Hopper et al.*, 2014; *Lekić and Fischer*, 2014; *Hopper et al.*, 2018]. For example, Sp receiver functions place this boundary at 55–65 km beneath the Snake River Plain, and at 60–80 km beneath the Basin and Range, the Rio Grande Rift and the Transition Zone. Beneath the Colorado Plateau, the putative base of the lithosphere appears to occur at 90–140 km depth [*Levander et al.*, 2011; *Kumar et al.*, 2012; *Levander and Miller*, 2012; *Hopper et al.*, 2014; *Lekić and Fischer*, 2014; *Hopper et al.*, 2018]. Using probabilistic inverse modeling of multiple observations, *Afonso et al.* [2016] predict lithospheric thicknesses at the edge of the Colorado Plateau that are in close agreement with those obtained from receiver functions. In the Rio Grande Rift, compositions of mantle xenoliths from ∼45 km depth are characteristic of both Proterozoic sub-continental lithosphere as well as of younger depleted upper mantle [*Byerly and Lassiter*, 2012]. *Gao et al.* [2004] associate the existence of anomalously slow velocities with lithospheric thinning. In contrast, mantle xenoliths from the Zuni-Bandera volcanic field in the Southern Transition Zone are exhumed from depths of 55–60 km. These xenoliths have sub-continental lithospheric mantle compositions [*Byerly and Lassiter*, 2012]. *Leeman and Rogers* [1970] and *Lachenbruch and Sass* [1977] use anomalous heatflow measurements to constrain melting depths in the Basin and Range and in the Rio Grande Rift to depths of 40–60 km.

The origin of thin lithosphere beneath western North America is poorly understood [see, e.g., *Kay and Mahlburg-Kay*, 1991; *Levander and Miller*, 2012; *Havlin et al.*, 2013]. There are two possible end-members. First, continental lithosphere beneath western North America may have been thinner than cratonic lithosphere for ∼0.5 Ga. Secondly, thick lithosphere may have been thinned, which is more likely for stratigraphic reasons. Thick piles of Paleozoic sedimentary rocks are recorded across North America and near identical strata can be traced from the Grand Canyon area toward the center of the continent [e.g. Illinois and Michigan basins; *Cross and Pilger*, 1978]. Marine sedimentary rocks of the Late Cretaceous Seaway demonstrate that tracts of western North America were below sea level until ∼70 Ma, after which regional uplift occurred [*Roberts and Kirschbaum*, 1995]. Rapid removal of the lower portion of the lithosphere might occur by thermal erosion, as a result of the growth of Rayleigh-Taylor instabilities [*Houseman et al.*, 1981; *Conrad and Molnar*, 1997; *Lee et al.*, 2001].

549 ### 4.2 Other Temperature Estimates

550 *Lee et al.* [2009] developed a thermobarometric scheme based upon silica activity and
551 upon Mg exchange between olivine and melt, which can be used to constrain the temperature
552 and pressure of melting within the source region. They propose that melting within the San
553 Francisco volcanic field of the Western Transition Zone takes place at a mantle potential tem-
554 perature of 1480 °C beneath a lithospheric plate that is 120–150 km thick. In the western Basin
555 and Range, they argue that basaltic melts are produced at temperatures of 1350–1450 °C and
556 depths of 60–90 km. *Reid et al.* [2012] apply the same thermobarometer to basaltic samples
557 from the Transition Zone fringing the Colorado Plateau. Based upon the results of *Li et al.* [2008],
558 they assumed that these melts have a water content of 0.05 wt%. They report mantle poten-
559 tial temperatures of $>$ 1465 °C at depths that are mostly shallower than 75 km. *Plank and Forsyth*
560 [2016] adapted the expressions of *Lee et al.* [2009], specifically to exploit a more accurate pa-
561 rameterization of the role of volatiles during melting, and obtained largely similar results. By
562 taking into account water and CO_2 concentrations of basaltic melts, they calculated potential
563 temperatures of $\sim$1300–1500 °C, with an average value of $\sim$1370 °C, at depths of 55–75 km
564 across the Basin and Range and Western Transition Zone.

565 We have applied the method of *Lee et al.* [2009] to our screened database and find that
566 samples from the Western Transition Zone yield temperatures of 1470–1500 °C at $\sim$70 km
567 depth. These values are consistent with the results of *Lee et al.* [2009] but require that the bulk
568 of melting occurs within the garnet stability field, in contrast to our conclusions. Samples from
569 the Basin and Range and from the Rio Grande Rift yield similar, or slightly lower, temper-
570 atures and pressures. For the Snake River Plain, the thermobarometric scheme yields a litho-
571 spheric thickness of $\sim$55 km and mantle potential temperatures of $>$ 1500 °C. The approach
572 of *Lee et al.* [2009] assumes that all melt equilibrates at a single pressure, in contrast to the
573 polybaric fractional melting approach. Furthermore, it is well known that this thermobarom-
574 eter is very sensitive to the Fe^{3+}/Fe^{T} ratio. An average Fe^{3+}/Fe^{T} ratio of 0.2 for western North
575 America is reported for samples $<$ 5 Ma old from the NAVDAT database, which is consis-
576 tent with ratios reported by *Plank and Forsyth* [2016] for the Basin and Range and for the West-
577 ern Transition Zone. In contrast, [*Lee et al.*, 2009] use a ratio of 0.1. Recalculated tempera-
578 tures for our screened database using Fe^{3+}/Fe^{T} = 0.2 are 50 °C lower and better match tem-
579 peratures predicted by our inverse modeling.

A range of alternative methodologies have been proposed. Here, we have also tested the PRIMELT-3 algorithm, which uses a mass balance approach to constrain primary magma compositions [*Herzberg and Asimow*, 2015]. This approach yields potential temperatures of 1340–1480 °C for our screened database with the greatest spread of temperatures obtained for the Snake River Plain samples. By applying the scheme of *Hole and Millett* [2016], we estimated final pressures and temperatures of melting, obtaining results that are similar to those of *Lee et al.* [2009]. *Rudzitis et al.* [2016] applied a different thermobarometric scheme based upon clinopyroxene fractionation to Western Transition Zone samples. They obtain crystallisation temperatures that are 100–200 °C lower than primary melt temperatures calculated by *Lee et al.* [2009]. We conclude that many strategies yield broadly similar ranges of mantle potential temperatures and depths of melting. Nevertheless, it is notable that inverse modeling of REE concentrations yields melting temperatures that are lower by up to 100 °C compared with thermobarometric temperature estimates. This systematic disparity is partly accounted for by variations in the ratio of Fe^{3+}/Fe^{T}.

4.3 Alternative Mechanisms of Melt Generation

Basaltic melting beneath continental lithosphere can be produced by elevating mantle temperature, thinning the lithosphere, and/or introducing volatiles to the source region [*Green and Ringwood*, 1967; *M^{c}Kenzie and Bickle*, 1988]. Distribution of volcanic activity across western North America is evidently correlated with the planform of shear wave velocity anomalies where lithospheric thickness is $<$100 km. However, melt fractions are significantly higher than those typically generated by melting of dry, peridotitic mantle at ambient potential temperatures. It is well known that hydration reduces melting temperatures by $\sim$50 °C [*Katz et al.*, 2003]. To assess the role that water could play in generating slow seismic anomalies, as well as accounting for the distribution and composition of observed volcanism, we used the alphaMELTS algorithm to generate forward models of melting at 0–4 GPa for mantle potential temperatures of 1250, 1300 and 1350 °C with source water contents of 0 to 10^4 ppm [*Ghiorso et al.*, 2002]. Assuming near-fractional isentropic melting and a residual porosity of 0.5%, we calculated trace element compositions, temperatures and melt fraction profiles, together with the changing water content of both source and melt. Shear wave velocity profiles are calculated using an appropriate correction for source water content [*Karato*, 2003].

We find that 10^4 ppm of water in the source region is required to give rise to a gradient change in REE concentrations that is similar to that produced by a temperature increase

of ∼50 °C. However, melt fraction distributions and $V_s(z)$ profiles are significantly different when water content is varied instead of temperature. In the hydrous example, the depth of onset of melting is deeper but the cumulative melt fraction remains similar to that generated by dry melting at the same temperature. Since water content decreases rapidly with continued melting, seismic velocities first increase with decreasing depth due to loss of water before slowly declining with decreasing pressure, once water is exhausted from the source. Dry melting at higher temperatures also leads to deepening of the onset of melting but produces much larger cumulative melt fractions and a smoother velocity profile that decreases with pressure. With regard to inverse modeling of REE compositions, a significantly hydrated source region could be simulated with a much more enriched source composition and/or with a low melt fraction tail within the garnet field but no change in the potential temperature estimate (i.e. final melt fraction and depth of melting). We conclude that the presence of minor amounts of water within the mantle do not significantly change our results.

We cannot entirely preclude water as a contributing factor to mantle melting beneath western North America. There are, however, several arguments suggesting that water content does not play a significant role with regard to the modeling of analyses presented here. There is undisputed evidence for water in the source region beneath the Basin and Range and beneath the Colorado Plateau, based upon melt inclusion observations [e.g. *Plank and Forsyth*, 2016; *Gazel et al.*, 2012], upon geochemical signatures [e.g. *Reid et al.*, 2012; *Rudzitis et al.*, 2016], and upon the presence of water in nominally anhydrous minerals of xenoliths [*Li et al.*, 2008]. However, those who favor the importance of water content for generation of basaltic volcanism in these regions also agree that temperature anomalies are required [e.g. *Dixon et al.*, 2004]. There is a consensus that some combination of long-lived hydration of the upper mantle caused by the presence of the subducting Farallon plate and temperature anomalies are needed in order to account for geochemical observations. If water content were the primary cause of melting, a homogeneous distribution of water within the upper mantle over a considerable area would be required. This signature would necessarily have to be either preserved or constantly replenished during the 80 Ma period over which volcanism has occurred. Furthermore, water content can only affect the initial stages of melting— it starts deeper and compositions are more enriched than for dry melting at the same temperature but the cumulative melt fraction is almost identical.

Finally, if a pyroxenite source is assumed, melt productivity increases without requiring anomalously elevated mantle temperatures [e.g. *Hirschmann et al.*, 2003]. Pyroxenite is

significantly more fusible than peridotite, which means that melting is initiated at greater depths leading to the generation of larger melt fractions throughout the entire melting column. *Reid et al.* [2012] and *Rudzitis et al.* [2016] suggest that the mantle source region for representative primitive basalts from the San Francisco and Mormon Mountain Volcanic Fields of the Western Transition Zone is predominantly peridotitic, based upon Hf-Nd isotopic ratios, as well as Zn/Fe and Fe/Mn ratios for olivine. Our screened database was carefully selected on the basis of its similarity to OIB compositions, which are thought to be primarily derived from peridotitic sources [*Shorttle et al.*, 2014]. If the approach of *Shorttle and Maclennan* [2011] is applied, which uses major elemental compositions to constrain potential end-member sources, our screened samples are inferred to have been generated by melting of dry lherzolitic rocks.

4.4 Regional Uplift & Heatflow

Isostatic calculations help to gauge whether or not our estimates of mantle temperature and lithospheric thickness are sufficient to generate the elevated topography of western North America (Figure 11). Following the approach of *McNab et al.* [2018] and many published contributions, we balance idealized columns of continental lithosphere against the density structure of a mid-ocean ridge. Elevation, e, of continental lithosphere is given by

$$e = t_w\Big(\frac{\rho_w - \rho_a}{\rho_{ca}}\Big) + t_{oc}\Big(\frac{\rho_{oc} - \rho_a}{\rho_{ca}}\Big) + t_{cc}\Big(\frac{\rho_m - \rho_{cc}}{\rho_{ca}}\Big) + 200\Big(\frac{\rho_a - \rho_{ca}}{\rho_{ca}}\Big) - t_m\Big(\frac{\rho_m - \rho_{ca}}{\rho_{ca}}\Big), \quad (4)$$

where $t_w = 2.8$ km and $\rho_w = 1$ Mg m^{-3} are the thickness and density of water at the mid-ocean ridge, $t_{oc} = 7.1$ km, $\rho_{oc} = 2.86$ Mg m^{-3} and $t_{cc} = 35$–50 km, $\rho_{cc} = 2.8$ Mg m^{-3} are variable thicknesses and densities of oceanic and continental crust, respectively. The variable lithospheric thickness, $t_m = 60$–200 km. ρ_m, ρ_a and ρ_{ca} are densities of lithospheric mantle and of asthenospheric mantle beneath the mid-ocean ridge and beneath continental lithosphere, respectively. Their values depend upon temperature and are calculated using $\rho_T = \rho_0(1 - \alpha T)$ where $\alpha = 3.15 \times 10^{-5}$ °C^{-1} and $\rho_0 = 3.33$ Mg m^{-3} is the density of mantle material at $T = 0$ °C. Note that ρ_a and ρ_{ca} differ in order to account for the putative thermal anomaly beneath western North America. The value of 200 km refers to the compensation depth which is taken to be the typical thickness of cratonic lithosphere beneath central North America.

First, we calculate the value of e for each of the ten volcanic provinces shown in Figure 7, using values of mantle potential temperature and lithospheric thickness determined by geochemical inverse modeling. At each location, average densities of lithospheric and astheno-

675 spheric mantle are determined by assuming a simple linear gradient and an adiabatic gradi-
676 ent, respectively. The effects of thermal expansion and compressibility were taken into account.
677 Chemical depletion of continental lithospheric mantle due to extraction of 1.5% melt was ac-
678 counted for by reducing its density by 15 kg m^{-3} [*Crosby et al.*, 2010]. The crustal thickness
679 profile is extracted from the model of *Shen and Ritzwoller* [2016] and the average crustal den-
680 sity is taken to be 2.8 Mg m^{-3} which is in close agreement with the results of *Schmandt et al.*
681 [2015]. At each location, lithospheric thickness is varied by $\pm$10 km and mantle potential tem-
682 perature by $\pm$20 °C, and in this way a mean elevation and its standard deviation are computed.
683 Secondly, we have constructed profiles at regular intervals along a curved transect that inter-
684 sects the principal volcanic provinces under consideration and terminates at the craton. On these
685 profiles, crustal thickness is also taken from *Shen and Ritzwoller* [2016] but lithospheric thick-
686 nesses are set in accordance with the results of *Hopper et al.* [2018] for western North Amer-
687 ica and of *Priestley and M^{c}Kenzie* [2013] for the cratonic regions. Mantle densities are esti-
688 mated by converting V_s profiles from the SL2013NA model into temperature and density. Litho-
689 spheric thickness beneath the craton is varied by $\pm$25 km.

690 Elevations calculated in these two ways agree to within $\sim$300 m and match the observed
691 topography to better than 500 m with three exceptions (Figure 11c). Large misfits occur at the
692 transition between western and cratonic North America toward the eastern end of this tran-
693 sect, on the Colorado Plateau, and adjacent to the Great Plains volcanic province. These mis-
694 fits arise from uncertainties in lithospheric thickness, thermal or density structure, as well as
695 the assumption of a simplified crustal structure [*Rodgers et al.*, 2002; *Hopper et al.*, 2018]. Across
696 western North America, the proportion of elevation that is generated and maintained by as-
697 thenospheric thermal anomalies appears to be $<$300 m, in agreement with previous isostatic
698 studies [*Levandowski et al.*, 2014, 2018]. We infer that the bulk of the topographic difference
699 between western and cratonic North America is caused by a $\sim$100 km difference in lithospheric
700 thickness. A contribution from mantle flow is not specifically required to match these obser-
701 vations in agreement with *Roy et al.* [2009], *Hyndman and Currie* [2011] and *Afonso et al.* [2016].

702 The distribution of heatflow anomalies broadly matches the pattern of Cenozoic basaltic
703 magmatism and of shear wave velocity anomalies [Figure 11; *Christiansen and Yeats*, 1992;
704 *Pollack et al.*, 1993]. *Lee and Uyeda* [1965] and *Roy et al.* [1968] showed that heatflow mea-
705 surements are twice as high as the continental average. For example, heatflow through the Snake
706 River Plain is about 100 mW m^{-2} with geothermal gradients as high as $\sim$70 °C km^{-1}. These
707 values increase eastward toward Yellowstone [*Blackwell*, 1989]. Average surface heatflow across

the Colorado Plateau is 65 mW m^{-2} with values of ~83 mW m^{-2} near the Jemez lineament (e.g. Zuni-Bandera field, STZ) and ~95 mW m^{-2} within the central Rio Grande Rift [*Reiter and Mansure*, 1983; *Eggleston and Reiter*, 1984; *Reiter et al.*, 1986]. We calculate conductive heatflow at the surface for different columns of continental lithosphere using

$$\rho C_P \frac{\partial T}{\partial t} = \frac{-\partial Q}{\partial z} + A, \tag{5}$$

where ρ is density, $C_P = 1.2 \times 10^3$ J mol^{-1} is specific heat capacity, and $A = 0.75$ μW m^{-3} is crustal heat production [*Michaut et al.*, 2009; *M^{c}Kenzie et al.*, 2005]. Heatflow, Q, is related to the continental temperature gradient by

$$Q = -k \frac{\partial T}{\partial z}, \tag{6}$$

where k is thermal conductivity. Average mantle density is calculated directly from the assumed temperature structure. Thermal conductivity is assumed to vary as a function of temperature. Within the mantle, $k(T)$ is parameterized using conductivity measurements of olivine [*Xu et al.*, 2004]. In the crust, the experimentally constrained expression of *Whittington et al.* [2009] is employed. In this way, surface heatflow is calculated both for lithospheric columns within each of the ten volcanic provinces shown in Figure 7 and for the transect shown in Figure 11a. At appropriate spot locations, we used temperature and lithospheric thickness estimates from geochemical inverse modeling. Along the transect, we use temperature estimates derived from the SL2013NA tomographic model of *Schaeffer and Lebedev* [2014]. Lithospheric thicknesses are from *Priestley and M^{c}Kenzie* [2013] and *Hopper et al.* [2018].

We calculate an average surface heatflow of 65–80 mW m^{-2} for western North America and of 50–60 mW m^{-2} for cratonic lithosphere (Figure 11d). Estimates determined from the results of geochemical inverse modeling are consistently higher than those determined from tomographic and receiver function models. This difference of ~30 mW m^{-2} appears to be resolvable and probably reflects the presence of a thermal anomaly beneath a thin plate. We acknowledge that these heat flow calculations are simplistic and do not account for any lateral heterogeneities of internal heat production. In the Basin and Range and Snake River Plain provinces, the existence of significant sediment-filled basins and shallow aquifers act to reduce surface heatflow measurements [*Blackwell*, 1989]. A detailed treatment of near-surface conductivity structure would probably yield better fits to heatflow observations but it is beyond the scope of this investigation. We conclude that a combination of elevated asthenospheric temperature and thin lithosphere significantly elevates surface heatflow.

5 Conclusions

We analyze and model a comprehensive database of Cenozoic basaltic volcanic rocks from western North America. Our principal aim is to show that rare earth and other incompatible trace element measurements can be used to determine melt fraction as a function of depth, which enables asthenospheric temperature and plate thickness to be estimated. Basaltic magmatism is generated by adiabatic decompression at, or close to, the spinel-garnet transition zone. The average lithospheric thickness constrained by rare earth element inverse modeling is 55 ± 10 km with melt generation beneath the Colorado Plateau being as deep as 70 ± 10 km and melt generation beneath the Snake River Plain being as shallow as 50 ± 10 km. Most of this melting occurs at depths shallower than $\sim$70 km. The average mantle potential temperature is 1340 ± 20 °C which is slightly hotter than the ambient asthenospheric value of ~ 1330 °C. Potential temperatures as high as 1365 °C occur beneath the Snake River Plain but the Colorado Plateau is underlain by mantle of ambient temperature.

These geochemical results are compared with shear wave velocity anomalies from a suite of regional and global tomographic models. We find that there is a positive correlation between shear wave velocities and trace element ratios, such as La/Yb, which act as proxies for the degree of melting. This correlation is confirmed by using an empirical calibration method to convert shear wave velocities into sub-plate temperatures. Seismically determined potential temperatures broadly agree with potential temperatures constrained by geochemical inverse modeling. We believe that this result is not significantly affected by variations in source rock composition, or by the presence of water in the source region.

Simple isostatic calculations highlight the overall consistency between regional epeirogeny, anomalously slow shear wave velocities, thinner lithosphere, and elevated heatflow across western North America. This consistency implies that sub-vertical mantle flow may not be a necessary prerequisite for generating and maintaining the observed regional topography. Instead, a combination of thin lithosphere and moderately elevated mantle potential temperature could be sufficient to explain $\sim$2 km of regional elevation. The existence of temperature anomalies suggests that edge-driven convection along the cratonic lithospheric keel may not be the primary cause of regional uplift and basaltic volcanism. Instead, our results bolster the notion that in this instance large-scale dynamic topography is generated and maintained by temperature anomalies within asthenospheric mantle directly beneath a thin plate.

Acknowledgments

We thank BP Exploration for supporting this research, which is part of the Parnaíba Basin Analysis Project. We are grateful to P. Ball, A. Bump, R. Clarke, M. Daly, J. Day, A. Dickinson, I. Frame, S. Gibson, M. Hoggard, E. Jennings, D. Lyness, F. McNab, D. Neave, N. Odling, N. Piggott, K. Priestley, F. Richards, G. Roberts, V. Rodríguez Tribaldos, O. Shorttle, S. Uhlemann and M. Walker for their help. T. Plank generously provided unpublished analytical measurements. Databases are listed in the references, tables and Supplementary Information. Cambridge Earth Sciences contribution esc.XXXX.

References

Afonso, J. C., N. Rawlinson, Y. Yang, D. L. Schutt, A. G. Jones, J. Fullea, and W. L. Griffin (2016), 3-D multiobservable probabilistic inversion for the compositional and thermal structure of the lithosphere and upper mantle: III. Thermochemical tomography in the Western-Central U.S., *Journal of Geophysical Research: Solid Earth*, *121*, 1–34, doi:10.1002/2016JB013049.

Anderson, R., D. M^{c}Kenzie, and J. Sclater (1973), Gravity, bathymetry and convection in the earth, *Earth and Planetary Science Letters*, *18*, 391–407.

Ashwal, L. D., and K. Burke (1989), African lithospheric structure, volcanism, and topography, *Earth and Planetary Science Letters*, *96*(1-2), 8–14, doi:10.1016/0012-821X(89)90119-2.

Ballmer, M. D., C. P. Conrad, E. I. Smith, and R. L. Johnsen (2015), Intraplate volcanism at the edges of the Colorado Plateau sustained by a combination of triggered edge-driven convection and shear-driven upwelling, *Geochemistry, Geophysics, Geosystems*, *16*, 1–14, doi:10.1002/2014GC005641.

Becker, T. W., C. Faccenna, E. D. Humphreys, A. R. Lowry, and M. S. Miller (2013), Static and dynamic support of western United States topography, *Earth and Planetary Science Letters*, *1*, 1–13, doi:10.1016/j.epsl.2013.10.012.

Blackwell, D. D. (1989), Regional implications of heat flow of the Snake River Plain, Northwestern United States, *Tectonophysics*, *164*(2-4), 323–343, doi:10.1016/0040-1951(89)90025-5.

Blundy, J. D., and B. J. Wood (2003), Partitioning of trace elements between crystals and melts, *Earth and Planetary Science Letters*, *210*(3-4), 383–397, doi:10.1016/S0012-821X(03)00129-8.

Bradshaw, T., C. J. Hawkesworth, and K. Gallagher (1993), Basaltic volcanism in the southern Basin and Range: No role for a mantle plume, *Earth and Planetary Science Letters*, *116*, 45–62, doi:10.1016/0012-821X(93)90044-A.

Brodie, J., D. Latin, and N. White (1994), Rare earth element inversion for melt distribution: sensivity and application, *Journal of Petrology*, *35*(4), 1155–1174, doi:10.1093/petrology/35.4.1155.

Bruinsma, S. L., C. Förste, O. Abrikosov, J.-M. Lemoine, J.-C. Marty, S. Mulet, M.-H. Rio, and S. Bonvalot (2014), ESA's satellite-only gravity field model via the direct approach based on all GOCE data, *Geophysical Research Letters*, *41*, 7508–7514, doi:10.1002/2014GL062045.

Burdick, S., R. D. van der Hilst, F. L. Vernon, V. Martynov, T. Cox, J. Eakins, G. H. Karasu, J. Tylell, L. Astiz, and G. L. Pavlis (2014), Model Update January 2013: Upper Mantle Heterogeneity beneath North America from Travel-Time Tomography with Global and USArray Transportable Array Data, *Seismological Research Letters*, *85*(1), 77–81, doi:10.1785/0220130098.

Byerly, B. L., and J. C. Lassiter (2012), Evidence from mantle xenoliths for lithosphere removal beneath the central Rio Grande Rift, *Earth and Planetary Science Letters*, *355-356*, 82–93, doi:10.1016/j.epsl.2012.08.034.

Camp, V. E., and B. B. Hanan (2008), A plume-triggered delamination origin for the Columbia River Basalt Group, *Geosphere*, *4*(3), 480–495, doi:10.1130/GES00175.1.

Chapin, C., M. Wilks, and W. McIntosh (2004), Space-time patterns of Late Cretaceous to present magmatism in New MexicoComparison with Andean volcanism and potential for future volcanism, *New Mexico Bureau of Geology & Mineral Resources, Bulletin*, *160*, 13–40.

Christiansen, R. L., and R. S. Yeats (1992), Post-Laramide geology of the U.S. Cordilleran region, *Geological Society of America*, pp. 261–406.

Conrad, C. P., and P. Molnar (1997), The growth of RayleighTaylor-type instabilities in the lithosphere for various rheological and density structures, *Geophysical Journal International*, *129*(1), 95–112, doi:10.1111/j.1365-246X.1997.tb00939.x.

Craig, H., J. E. Lupton, J. A. Welhan, and R. J. Poreda (1978), Helium isotope ratios in Yellowstone and Lassen Park volcanic gases, *Geophysical Research Letters*, *5*(11), 897–900, doi:10.1029/GL005i011p00897.

Crosby, A. G., S. Fishwick, and N. White (2010), Structure and evolution of the intracratonic Congo Basin, *Geochemistry, Geophysics, Geosystems*, *11*(6), 1–20, doi:10.1029/2009GC003014.

Cross, T. A., and R. H. Pilger (1978), Tectonic controls of late Cretaceous sedimentation, western interior, USA, *Nature*, *274*(5672), 653–657, doi:10.1038/274653a0.

Crow, R. S., K. E. Karlstrom, Y. Asmerom, B. Schmandt, V. Polyak, and S. A. DuFrane (2010), Shrinking of the Colorado Plateau via lithospheric mantle erosion: Evidence from Nd and Sr isotopes and geochronology of Neogene basalts, *Geology*, *39*(1), 27–30, doi:10.1130/G31611.1.

Dixon, J. E., T. H. Dixon, D. R. Bell, and R. Malservisi (2004), Lateral variation in upper mantle viscosity: Role of water, *Earth and Planetary Science Letters*, *222*(2), 451–467, doi:10.1016/j.epsl.2004.03.022.

Eggins, S. M., J. D. Woodhead, L. P. J. Kinsley, G. E. Mortimer, P. J. Sylvester, M. T. McCulloch, J. M. Hergt, and M. R. Handler (1997), A simple method for the precise determination of $>$ 40 trace elements in geological samples by ICPMS using enriched isotope internal standardisation, *Chemical Geology*, *1*(4), 311–326, doi:http://dx.doi.org/10.1016/S0009-2541(96)00100-3.

Eggleston, R. E., and M. Reiter (1984), Terrestrial heat-flow estimates from petroleum bottom-hole temperature data in the Colorado Plateau and the eastern Basin and Range Province., *Geological Society of America Bulletin*, *95*(9), 1027–1034, doi:10.1130/0016-7606(1984)95¡1027:THEFPB¿2.0.CO;2.

Faul, U. H., and I. Jackson (2007), Diffusion creep of dry, melt-free olivine, *Journal of Geophysical Research: Solid Earth*, *112*(4), 1–14, doi:10.1029/2006JB004586.

Fitton, J. G., D. E. James, and W. P. Leeman (1991), Basic magmatism associated with Late Cenozoic extension in the western United States: Compositional variations in space and time, *Journal of Geophysical Research*, *96*(B8), 13,693–13,711, doi:10.1029/91JB00372.

Fitton, J. G., A. D. Saunders, L. Larsen, B. Hardarson, and M. J. Norry (1998), Volcanic rocks from the southeast Greenland Margin at 63N: composition, petrogenesis, and mantle sources, in *Proceedings of the Ocean Drilling Program, 152 Scientific Results*, vol. 152, pp. 331–350, Ocean Drilling Program, doi:10.2973/odp.proc.sr.152.233.1998.

Flament, N., M. Gurnis, and R. D. Müller (2013), A review of observations and models of dynamic topography, *Lithosphere*, *5*(2), 189–210, doi:10.1130/L245.1.

Galloway, W. E., T. L. Whiteaker, and P. Ganey-Curry (2011), History of Cenozoic North American drainage basin evolution, sediment yield, and accumulation in the Gulf of Mexico basin, *Geosphere*, *7*(4), 938–973, doi:10.1130/GES00647.1.

Gao, W., S. P. Grand, W. S. Baldridge, D. Wilson, M. West, J. F. Ni, and R. C. Aster (2004), Upper mantle convection beneath the central Rio Grande rift imaged by P and S wave tomography, *Journal of Geophysical Research*, *109*(B3), 1–16, doi: 10.1029/2003JB002743.

Gazel, E., T. Plank, D. W. Forsyth, C. Bendersky, C.-T. A. Lee, and E. H. Hauri (2012), Lithosphere versus asthenosphere mantle sources at the Big Pine Volcanic Field, California, *Geochemistry, Geophysics, Geosystems*, *13*(1), 1–25, doi: 10.1029/2012GC004060.

Ghiorso, M. S., M. M. Hirschmann, P. W. Reiners, and V. C. Kress (2002), The pMELTS: A revision of MELTS for improved calculation of phase relations and major element partitioning related to partial melting of the mantle to 3 GPa, *Geochemistry Geophysics Geosystems*, *3*(5), 1–36, doi:10.1029/2001gc000217.

Goes, S., and S. Van Der Lee (2002), Thermal structure of the North American uppermost mantle inferred from seismic tomography, *Journal of Geophysical Research*, *107*(B3), 1–13, doi:10.1029/2000JB000049.

Graham, D. W., M. R. Reid, B. T. Jordan, A. L. Grunder, W. P. Leeman, and J. E. Lupton (2009), Mantle source provinces beneath the Northwestern USA delimited by helium isotopes in young basalts, *Journal of Volcanology and Geothermal Research*, *188*(1-3), 128–140, doi:10.1016/j.jvolgeores.2008.12.004.

Green, D. H., and A. E. Ringwood (1967), The genesis of basaltic magmas, *Contributions to Mineralogy and Petrology*, *15*(2), 103–190, doi:10.1007/BF00372052.

Green, E. C. R., T. J. B. Holland, R. Powell, and R. W. White (2012), Garnet and spinel lherzolite assemblages in MgO-Al2O3-SiO2 and CaO-MgO-Al2O3-SiO2: thermodynamic models and an experimental conflict, *Journal of Metamorphic Geology*, *30*(6), 561–577, doi:10.1111/j.1525-1314.2012.00981.x.

Gripp, A. E., and R. G. Gordon (2002), Young tracks of hotspots and current plate velocities, *Geophysical Journal International*, *150*(2), 321–361, doi:10.1046/j.1365-246X.2002.01627.x.

Hager, B. H., and M. A. Richards (1989), Long-Wavelength Variations in Earth's Geoid: Physical Models and Dynamical Implications, *Philosophical Transactions of the Royal*

Society A: Mathematical, Physical and Engineering Sciences, *328*(1599), 309–327, doi: 10.1098/rsta.1989.0038.

Hammond, W. C., and E. D. Humphreys (2000), Upper mantle seismic wave attenuation: Effects of realistic partial melt distribution, *Journal of Geophysical Research*, *105*(B5), 10,987–10,999, doi:10.1029/2000jb900042.

Hanan, B. B., J. W. Shervais, and S. K. Vetter (2008), Yellowstone plumecontinental lithosphere interaction beneath the Snake River Plain, *Geology*, *36*(1), 51–54, doi: 10.1130/G23935A.1.

Hansen, S. M., K. G. Dueker, J. C. Stachnik, R. C. Aster, and K. E. Karlstrom (2013), A rootless rockies - Support and lithospheric structure of the Colorado Rocky Mountains inferred from CREST and TA seismic data, *Geochemistry, Geophysics, Geosystems*, *14*(8), 2670–2695, doi:10.1002/ggge.20143.

Havlin, C., E. M. Parmentier, and G. Hirth (2013), Dike propagation driven by melt accumulation at the lithosphere - asthenosphere boundary, *Earth and Planetary Science Letters*, *376*, 20–28, doi:10.1016/j.epsl.2013.06.010.

Herzberg, C. T., and P. D. Asimow (2015), PRIMELT3 MEGA.XLSM software for primary magma calculation: Peridotite primary magma MgO contents from the liquidus to the solidus, *Geochemistry, Geophysics, Geosystems*, *16*, 563–578, doi: 10.1002/2014GC005631.Received.

Hirschmann, M. M., T. Kogiso, M. B. Baker, and E. M. Stolper (2003), Alkalic magmas generated by partial melting of garnet pyroxenite, *Geology*, *31*(6), 481–484, doi: 10.1130/0091-7613(2003)031¡0481:AMGBPM¿2.0.CO;2.

Hole, M. J., and J. M. Millett (2016), Controls of Mantle Potential Temperature and Lithospheric Thickness on Magmatism in the North Atlantic Igneous Province, *Journal of Petrology*, *57*(2), 417–436, doi:10.1093/petrology/egw014.

Hopper, E., and K. M. Fischer (2018), The Changing Face of the LithosphereAsthenosphere Boundary: Imaging Continental Scale Patterns in upper mantle structure across the contiguous U.S. with Sp Converted Waves, *Geochemistry, Geophysics, Geosystems*, Accepted Author Manuscript, doi:10.1029/2018GC007476.

Hopper, E., H. A. Ford, K. M. Fischer, V. Lekić, and M. J. Fouch (2014), The lithosphereasthenosphere boundary and the tectonic and magmatic history of the northwestern United States, *Earth and Planetary Science Letters*, *1*, 1–13, doi: 10.1016/j.epsl.2013.12.016.

Houseman, G. A., D. M^{c}Kenzie, and P. Molnar (1981), Convective instability of a thickened boundary layer and its relevance for the thermal evolution of continental convergence belts, *Journal of Geophysical Research: Solid Earth*, *86*(B7), 6115–6132, doi:10.1029/JB086iB07p06115.

Huang, H.-H., F.-C. Lin, B. Schmandt, J. Farrell, R. B. Smith, and V. C. Tsai (2015), The Yellowstone magmatic system from the mantle plume to the upper crust, *Science*, *348*(6236), 773–776, doi:10.1002/2014GL059588.

Humphreys, E. D. (1995), Post-Laramide removal of the Farallon slab, western United States, *Geology*, *23*(11), 987–990, doi:10.1130/0091-7613(1995)023¡0987:PLROTF¿2.3.CO;2.

Humphreys, E. D., E. Hessler, K. G. Dueker, G. L. Farmer, E. Erslev, and T. Atwater (2003), How Laramide-Age Hydration of North American Lithosphere by the Farallon Slab Controlled Subsequent Activity in the Western United States, *International Geology Review*, *45*, 575–595, doi:10.2747/0020-6814.45.7.575.

Hyndman, R. D., and C. A. Currie (2011), Why is the North America Cordillera high? Hot backarcs, thermal isostasy, and mountain belts, *Geology*, *39*(8), 783–786, doi:10.1130/G31998.1.

James, D. E., M. J. Fouch, R. W. Carlson, and J. B. Roth (2011), Slab fragmentation, edge flow and the origin of the Yellowstone hotspot track, *Earth and Planetary Science Letters*, *311*(1-2), 124–135, doi:10.1016/j.epsl.2011.09.007.

Jennings, E. S., and T. J. B. Holland (2015), A Simple Thermodynamic Model for Melting of Peridotite in the System NCFMASOCr, *Journal of Petrology*, *56*(5), 869–892, doi:10.1093/petrology/egv020.

Jordan, B. T. (2002), Basaltic Volcanism and Tectonics of the High Lava Plains, Southeastern Oregon, Ph.D. thesis, Oregon State University.

Karato, S.-i. (2003), Mapping water content in the upper mantle, *Geophysical Monograph Series*, *138*, 135–152, doi:10.1029/138GM08.

Katz, R. F., M. Spiegelman, and C. H. Langmuir (2003), A new parameterization of hydrous mantle melting, *Geochemistry, Geophysics, Geosystems*, *4*(9), 1–19, doi:10.1029/2002GC000433.

Kay, R. W., and S. Mahlburg-Kay (1991), Creation and destruction of lower continental crust, *Geologische Rundschau*, *80*(2), 259–278, doi:10.1007/BF01829365.

963 Kempton, P. D., J. G. Fitton, C. J. Hawkesworth, and D. S. Ormerod (1991), Isotopic and
964 trace element constraints on the composition and evolution of the lithosphere beneath
965 the southwestern United States, *Journal of Geophysical Research*, *96*(B8), 13,713–
966 13,735, doi:10.1029/91JB00373.
967 Kennedy, B. M., and M. C. van Soest (2007), Flow of mantle fluids through
968 the ductile lower crust: helium isotope trends., *Science*, *318*, 1433–1436, doi:
969 10.1126/science.1147537.
970 Kennedy, B. M., M. A. Lynch, J. H. Reynolds, and S. P. Smith (1985), Intensive sam-
971 pling of noble gases in fluids at Yellowstone: I. Early overview of the data; regional
972 patterns, *Geochimica et Cosmochimica Acta*, *49*(5), 1251–1261, doi:10.1016/0016-
973 7037(85)90014-6.
974 Klemme, S., and H. S. C. O'Neill (2000), The near-solidus transition from garnet lher-
975 zolite to spinel lherzolite, *Contributions to Mineralogy and Petrology*, *138*, 237–248,
976 doi:10.1007/s004100050560.
977 Kojitani, H., and M. Akaogi (1997), Melting enthalpies of mantle peridotite: calorimet-
978 ric determinations in the system CaO-MgO-Al2O3-SiO2 and application to magma
979 generation, *Earth and Planetary Science Letters*, *153*(3-4), 209–222, doi:10.1016/S0012-
980 821X(97)00186-6.
981 Kumar, P., X. Yuan, R. Kind, and J. Mechie (2012), The lithosphere-asthenosphere
982 boundary observed with USArray receiver functions, *Solid Earth*, *3*(1), 149–159, doi:
983 10.5194/se-3-149-2012.
984 Lachenbruch, A., and J. Sass (1977), Heat flow in the United States and the thermal
985 regime of the crust, in *The Nature and Physical Properties of the Earth's Crust*, vol. 20,
986 pp. 626–675, American Geophysical Union, doi:10.1029/GM020p0626.
987 Leat, P., R. Thompson, M. Morrison, G. Hendry, and A. P. Dickin (1991), Alkaline hybrid
988 mafic magmas of the Yampa area, NW Colorado, and their relationship to the Yellow-
989 stone mantle plume and lithospheric mantle domains, *Contributions to Mineralogy and*
990 *Petrology*, *107*(3), 310–327, doi:10.1007/BF00325101.
991 Lee, C.-T. A., R. L. Rudnick, and G. H. Brimhall (2001), Deep lithospheric dy-
992 namics beneath the Sierra Nevada during the Mesozoic and Cenozoic as inferred
993 from xenolith petrology, *Geochemistry, Geophysics, Geosystems*, *2*(12), 1–27, doi:
994 10.1029/2001GC000152.

Lee, C.-T. A., P. Luffi, T. Plank, H. Dalton, and W. P. Leeman (2009), Constraints on the depths and temperatures of basaltic magma generation on Earth and other terrestrial planets using new thermobarometers for mafic magmas, *Earth and Planetary Science Letters*, *279*(1-2), 20–33, doi:10.1016/j.epsl.2008.12.020.

Lee, W. H. K., and S. Uyeda (1965), Review of heat flow data, in *Terrestrial heat flow*, pp. 87–190, American Geophysical Union, doi:10.1029/GM008p0087.

Leeman, W. P., and J. Rogers (1970), Late Cenozoic alkali-olivine basalts of the Basin-Range Province, USA, *Contributions to Mineralogy and Petrology*, *25*, 1–24, doi:10.1007/BF00383059.

Leeman, W. P., D. L. Schutt, and S. S. Hughes (2009), Thermal structure beneath the Snake River Plain: Implications for the Yellowstone hotspot, *Journal of Volcanology and Geothermal Research*, *188*(1-3), 57–67, doi:10.1016/j.jvolgeores.2009.01.034.

Lekić, V., and K. M. Fischer (2014), Contrasting lithospheric signatures across the western United States revealed by Sp receiver functions, *Earth and Planetary Science Letters*, *402*, 90–98, doi:10.1016/j.epsl.2013.11.026.

Levander, A., and M. S. Miller (2012), Evolutionary aspects of lithosphere discontinuity structure in the Western U.S., *Geochemistry, Geophysics, Geosystems*, *13*(1), 1–22, doi:10.1029/2012GC004056.

Levander, A., B. Schmandt, M. S. Miller, K. H. Liu, K. E. Karlstrom, R. S. Crow, C.-T. A. Lee, and E. D. Humphreys (2011), Continuing Colorado plateau uplift by delamination-style convective lithospheric downwelling, *Nature*, *472*(7344), 461–5, doi:10.1038/nature10001.

Levandowski, W. B., C. H. Jones, L. A. Butcher, and K. H. Mahan (2018), Lithospheric density models reveal evidence for Cenozoic uplift of the Colorado Plateau and Great Plains by lower-crustal hydration, *Geosphere*, *14*(3), 1150–1164, doi:10.1130/GES01619.1.

Levandowski, W. B., C. H. Jones, W. Shen, M. H. Ritzwoller, and V. Schulte-Pelkum (2014), Origins of topography in the western U.S.: Mapping crustal and upper mantle density variations using a uniform seismic velocity model, *Journal of Geophysical Research: Solid Earth*, *119*, 2375–2396, doi:10.1002/2013JB010607.

Li, Z. X. A., C.-T. A. Lee, A. H. Peslier, A. Lenardic, and S. J. Mackwell (2008), Water contents in mantle xenoliths from the Colorado Plateau and vicinity: Implications for the mantle rheology and hydration-induced thinning of continental lithosphere, *Journal*

of Geophysical Research: Solid Earth, *113*(9), 1–22, doi:10.1029/2007JB005540.

Lin, F.-C., M. H. Ritzwoller, Y. Yang, M. P. Moschetti, and M. J. Fouch (2011), Complex and variable crustal and uppermost mantle seismic anisotropy in the western United States, *Nature Geoscience*, *4*(1), 55–61, doi:10.1038/ngeo1036.

Lithgow-Bertelloni, C., and P. G. Silver (1998), Dynamic topography, plate driving forces and the African superswell, *Nature*, *395*(September), 345–348, doi:10.1038/26212.

Liu, L., and M. Gurnis (2010), Dynamic subsidence and uplift of the Colorado Plateau, *Geology*, *38*(7), 663–666, doi:10.1130/G30624.1.

McCarthy, C., and Y. Takei (2011), Anelasticity and viscosity of partially molten rock analogue: Toward seismic detection of small quantities of melt, *Geophysical Research Letters*, *38*(18), 3–7, doi:10.1029/2011GL048776.

McCarthy, C., Y. Takei, and T. Hiraga (2011), Experimental study of attenuation and dispersion over a broad frequency range: 2. the universal scaling of polycrystalline materials, *Journal of Geophysical Research: Solid Earth*, *116*(9), 1–18, doi:10.1029/2011JB008384.

McDonough, W. F., and S. S. Sun (1995). The composition of the Earth, *Chemical Geology*, *120*, 223–253, doi:10.1016/0009-2541(94)00140-4.

M^{c}Kenzie, D. (2000), Constraints on melt generation and transport from U-series activity ratios, *Chemical Geology*, *162*(2), 81–94, doi:10.1016/S0009-2541(99)00126-6.

M^{c}Kenzie, D., and M. Bickle (1988), The volume and composition of melt generated by extension of the lithosphere, *Journal of Petrology*, *29*(3), 625–679, doi:10.1093/petrology/29.3.625.

M^{c}Kenzie, D., and R. K. O'Nions (1991), Partial melt distributions from inversion of rare earth element concentrations, *Journal of Petrology*, *32*, 1021–1091, doi:10.1093/petrology/32.5.1021.

M^{c}Kenzie, D., J. Jackson, and K. Priestley (2005), Thermal structure of oceanic and continental lithosphere, *Earth and Planetary Science Letters*, *233*(3-4), 337–349, doi:10.1016/j.epsl.2005.02.005.

McNab, F., P. Ball, M. J. Hoggard, and N. J. White (2018), Neogene Uplift and Magmatism of Anatolia: Insights from Drainage Analysis and Basaltic Geochemistry, *Geochemistry, Geophysics, Geosystems*, *19*, 1–39, doi:10.1002/2017GC007251.

Michaut, C., C. Jaupart, and J. C. Mareschal (2009), Thermal evolution of cratonic roots, *Lithos*, *109*(1-2), 47–60, doi:10.1016/j.lithos.2008.05.008.

Moucha, R., A. M. Forte, D. B. Rowley, J. X. Mitrovica, N. A. Simmons, and S. P. Grand (2008), Mantle convection and the recent evolution of the Colorado Plateau and the Rio Grande Rift valley, *Geology*, *36*(6), 439, doi:10.1130/G24577A.1.

Moucha, R., A. M. Forte, D. B. Rowley, J. X. Mitrovica, N. A. Simmons, and S. P. Grand (2009), Deep mantle forces and the uplift of the Colorado Plateau, *Geophysical Research Letters*, *36*(L19310), 1–6, doi:10.1029/2009GL039778.

Nelson, P. L., and S. P. Grand (2018), Lower-mantle plume beneath the Yellowstone hotspot revealed by core waves,*Nature Geoscience*, *11*, 280–284, doi:10.1038/s41561-018-0075-y.

Obrebski, M., R. M. Allen, F. F. Pollitz, and S.-H. Hung (2011), Lithosphere-asthenosphere interaction beneath the western United States from the joint inversion of body-wave traveltimes and surface-wave phase velocities, *Geophysical Journal International*, *185*(2), 1003–1021, doi:10.1111/j.1365-246X.2011.04990.x.

Parsons, B., and S. Daly (1983), The relationship between surface topography, gravity anomalies, and temperature structure of convection, *Journal of Geophysical Research*, *88*(B2), 1129–1144, doi:10.1029/JB088iB02p01129.

Parsons, T., G. A. Thompson, and N. H. Sleep (1994), Mantle plume influence on the Neogene uplift and extension of the US western Cordillera?, *Geology*, *22*, 83–86, doi:10.1130/0091-7613(1994)022¡0083.

Pearce, J. (1982), Trace element characteristics of lavas from destructive plate boundaries., in *Orogenic Andesites and Related Rocks*, edited by R. S. Thorpe, pp. 525 – 548, John Wiley & Sons.

Pierce, K. L., and L. A. Morgan (2009), Is the track of the Yellowstone hotspot driven by a deep mantle plume? Review of volcanism, faulting, and uplift in light of new data, *Journal of Volcanology and Geothermal Research*, *188*(1-3), 1–25, doi:10.1016/j.jvolgeores.2009.07.009.

Plank, T., and D. W. Forsyth (2016), Thermal structure and melting conditions in the mantle beneath the Basin and Range province from seismology and petrology, *Geochemistry, Geophysics, Geosystems*, *17*, 1–27, doi:10.1002/2015GC006205.

Pollack, H. N., S. J. Hurter, and J. R. Johnson (1993), Heat flow from the Earth's interior: Analysis of the global data set, *Reviews of Geophysics*, *31*(3), 267–280, doi:10.1029/93RG01249.

1093 Pollitz, F. F. (2008), Observations and interpretation of fundamental mode Rayleigh wave-
1094 fields recorded by the Transportable Array (USArray), *Journal of Geophysical Research:*
1095 *Solid Earth*, *113*(10), 1–24, doi:10.1029/2007JB005556.

1096 Porritt, R. W., R. M. Allen, and F. F. Pollitz (2014), Seismic imaging east of the Rocky
1097 Mountains with USArray, *Earth and Planetary Science Letters*, *402*, 16–25, doi:
1098 10.1016/j.epsl.2013.10.034.

1099 Press, W. H., S. A. Teukolsky, W. T. Vetterling, and B. P. Flannery (1992), *Numerical*
1100 *recipes in Fortran: the art of scientific computing*, Cambridge University Press.

1101 Priestley, K., and D. M^{c}Kenzie (2006), The thermal structure of the lithosphere from
1102 shear wave velocities, *Earth and Planetary Science Letters*, *244*(1-2), 285–301, doi:
1103 10.1016/j.epsl.2006.01.008.

1104 Priestley, K., and D. M^{c}Kenzie (2013), The relationship between shear wave velocity,
1105 temperature, attenuation and viscosity in the shallow part of the mantle, *Earth and*
1106 *Planetary Science Letters*, *381*, 78–91, doi:10.1016/j.epsl.2013.08.022.

1107 Refayee, H. A., B. B. Yang, K. H. Liu, and S. S. Gao (2013), Mantle flow and litho-
1108 sphereasthenosphere coupling beneath the southwestern edge of the North American
1109 craton: Constraints from shear-wave splitting measurements, *Earth and Planetary Sci-*
1110 *ence Letters*, *402*, 209–220, doi:10.1016/j.epsl.2013.01.031.

1111 Reid, M. R., R. A. Bouchet, J. Blichert-Toft, A. Levander, K. Liu, M. S. Miller, and F. C.
1112 Ramos (2012), Melting under the Colorado Plateau, USA, *Geology*, *40*(5), 387–390,
1113 doi:10.1130/G32619.1.

1114 Reiter, M., and A. J. Mansure (1983), Geothermal Studies in the San Juan Basin and
1115 the four Corners area of the Colorado Plateau I. Terrestrial heat-flow measurements,
1116 *Tectonophysics*, *91*, 233–251, doi:10.1016/0040-1951(83)90043-4.

1117 Reiter, M., R. E. Eggleston, B. R. Broadwell, and J. Minier (1986), Estimates of terrestrial
1118 heat flow from deep petroleum tests along the Rio Grande Rift in central and south-
1119 ern New Mexico, *Journal of Geophysical Research: Solid Earth*, *91*(B6), 6225–6245,
1120 doi:10.1029/JB091iB06p06225.

1121 Roberts, G. G., J. D. Paul, N. J. White, and J. Winterbourne (2012), Temporal and spa-
1122 tial evolution of dynamic support from river profiles: A framework for Madagascar,
1123 *Geochemistry, Geophysics, Geosystems*, *13*(4), 1–23, doi:10.1029/2012GC004040.

1124 Roberts, L. N., and M. A. Kirschbaum (1995), Paleogeography of the Late Cretaceous of
1125 the Western Interior of middle North America- coal distribution and sediment accumula-

tion, *Tech. rep.*, U.S. Geological Survey, doi:10.1016/0003-6870(73)90259-7.

Rodgers, D. W., H. T. Ore, R. T. Bobo, N. Mcquarrie, and N. Zentner (2002), Extension and Subsidence of the Eastern Snake River Plain, Idaho, *Idaho Geological Survey Bulletin*, *30*, 121–155.

Roy, M., T. H. Jordan, and J. L. Pederson (2009), Colorado Plateau magmatism and uplift by warming of heterogeneous lithosphere, *Nature*, *459*(7249), 978–82, doi:10.1038/nature08052.

Roy, R. F., E. R. Decker, D. D. Blackwell, and F. Birch (1968), Heat flow in the United States, *Journal of Geophysical Research*, *73*(16), 5207–5221, doi:10.1029/JB073i016p05207.

Rudzitis, S., M. R. Reid, and J. Blichert-Toft (2016), On edge melting under the Colorado Plateau margin, *Geochemistry Geophysics Geosystems*, *17*, 1–20, doi:10.1002/2015GC006060.Received.

Salters, V. J. M., and A. Stracke (2004), Composition of the depleted mantle, *Geochemistry, Geophysics, Geosystems*, *5*, 1–27, doi:10.1029/2003GC000597.

Saltus, R., and G. A. Thompson (1995), Why is it downhill from Tonopah to Las Vegas?: A case for mantle plume support of the high northern Basin and Range, *Tectonics*, *14*(6), 1235–1244, doi:10.1029/95TC02288.

Schaeffer, A., and S. Lebedev (2014), Imaging the North American continent using waveform inversion of global and USArray data, *Earth and Planetary Science Letters*, *402*, 26–41, doi:10.1016/j.epsl.2014.05.014.

Schmandt, B., and E. D. Humphreys (2010), Complex subduction and small-scale convection revealed by body-wave tomography of the western United States upper mantle, *Earth and Planetary Science Letters*, *297*(3-4), 435–445, doi:10.1016/j.epsl.2010.06.047.

Schmandt, B., and F.-C. Lin (2014), P and S wave tomography of the mantle beneath the United States, *Geophysical Research Letters*, *41*, 6342–6349, doi:10.1002/2014GL061231.

Schmandt, B., F.-C. Lin, and K. E. Karlstrom (2015), Distinct crustal isostasy trends east and west of the Rocky Mountain Front, *Geophysical Research Letters*, *42*(23), 10,290–10,298, doi:10.1002/2015GL066593.

Schutt, D.L. and C.E. Lesher, (2006), Effects of melt depletion on the density and seismic velocity of garnet and spinel lherzolite, *Journal of Geophysical Research: Solid Earth*, *111*(5), 1–24, doi:10.1029/2003JB002950.

1159 Sheehan, A. F., G. A. Abers, C. H. Jones, and A. L. Lernerlam (1995), Crustal Thick-
1160 ness Variations Across the Colorado Rocky-Mountain From Teleseismic Receiver
1161 Functions, *Journal of Geophysical Research-Solid Earth*, *100*(B10), 20,391–20,404,
1162 doi:10.1029/95jb01966.

1163 Shen, W., and M. H. Ritzwoller (2016), Crustal and uppermost mantle structure beneath
1164 the United States, *Journal of Geophysical Research: Solid Earth*, *121*, 4306–4342, doi:
1165 10.1002/2012JB010016.1.

1166 Shen, W., M. H. Ritzwoller, and V. Schulte-Pelkum (2013), A 3-D model of the crust and
1167 uppermost mantle beneath the Central and Western US by joint inversion of receiver
1168 functions and surface wave dispersion, *Journal of Geophysical Research: Solid Earth*,
1169 *118*(1), 262–276, doi:10.1029/2012JB009602.

1170 Shorttle, O., and J. Maclennan (2011), Compositional trends of Icelandic basalts: Implica-
1171 tions for short-length scale lithological heterogeneity in mantle plumes, *Geochemistry,*
1172 *Geophysics, Geosystems*, *12*(11), doi:10.1029/2011GC003748.

1173 Shorttle, O., J. Maclennan, and S. Lambart (2014), Quantifying lithological vari-
1174 ability in the mantle, *Earth and Planetary Science Letters*, *395*, 24–40, doi:
1175 10.1016/j.epsl.2014.03.040.

1176 Spencer, J. E. (1996), Uplift of the Colorado Plateau due to lithosphere attenuation during
1177 Laramide low-angle subduction, *Journal of Geophysical Research*, *101*, 13,595–13,609,
1178 doi:10.1029/96JB00818.

1179 Stracke, A., M. Bizimis, and V. J. M. Salters (2003), Recycling oceanic crust: Quantitative
1180 constraints, *Geochemistry, Geophysics, Geosystems*, *4*(3), doi:10.1029/2001GC000223.

1181 Stracke, A., A. W. Hofmann, and S. R. Hart (2005), FOZO, HIMU, and the rest
1182 of the mantle zoo, *Geochemistry, Geophysics, Geosystems*, *6*(5), 1–20, doi:
1183 10.1029/2004GC000824.

1184 Thompson, G. A., and M. L. Zoback (1979), Regional geophysics of the Colorado
1185 Plateau, *Tectonophysics*, *61*(1-3), 149–181, doi:10.1016/0040-1951(79)90296-8.

1186 Thompson, R., C. J. Ottley, P. M. Smith, D. G. Pearson, A. P. Dickin, M. Morrison,
1187 P. Leat, and S. Gibson (2005), Source of the Quaternary Alkalic Basalts, Picrites and
1188 Basanites of the Potrillo Volcanic Field, New Mexico, USA: Lithosphere or Convecting
1189 Mantle?, *Journal of Petrology*, *46*(8), 1603–1643, doi:10.1093/petrology/egi028.

1190 van Wijk, J. W., W. S. Baldridge, J. van Hunen, S. Goes, R. C. Aster, D. D. Coblentz,
1191 S. P. Grand, and J. F. Ni (2010), Small-scale convection at the edge of the Colorado

1192 Plateau: Implications for topography, magmatism, and evolution of Proterozoic litho-
1193 sphere, *Geology*, *38*(7), 611–614, doi:10.1130/G31031.1.

1194 Walter, M. J., T. Katsura, and A. Kubo (2002), Spinelgarnet lherzolite transition in the
1195 system CaO-MgO-Al2O3-SiO2 revisited: an in situ X-ray study, *Geochimica et Cos-*
1196 *mochimica acta*, *66*(12), 2109–2121, doi:10.1016/S0016-7037(02)00845-1.

1197 Welhan, J. A., R. J. Poreda, W. Rison, and H. Craig (1988), Helium isotopes in geother-
1198 mal and volcanic gases of the western United States, I. Regional variability and mag-
1199 matic origin, *Journal of Volcanology and Geothermal Research*, *34*(3-4), 185–199,
1200 doi:10.1016/0377-0273(88)90032-7.

1201 White, C. M., W. K. Hart, B. Bonnichsen, and D. Matthews (2004), Geochemical and
1202 Sr-isotopic variations in western Snake River plain basalts, Idaho, *Bulletin - Idaho*
1203 *Geological Survey*, *30*, 329–342.

1204 White, R. S., and D. M^{c}Kenzie (1995), Mantle plumes and flood basalts, *Journal of Geo-*
1205 *physical Research*, *100*(95), 17,543–17,585, doi:10.1029/95JB01585.

1206 White, R. S., D. M^{c}Kenzie, and R. K. O'Nions (1992), Oceanic crustal thickness from
1207 seismic measurements and rare earth element inversions, *Journal of Geophysical Re-*
1208 *search*, *97*(B13), 19,683–19,715, doi:10.1029/92JB01749.

1209 Whittington, A. G., A. M. Hofmeister, and P. I. Nabelek (2009), Temperature-dependent
1210 thermal diffusivity of the Earth's crust and implications for magmatism, *Nature*, *458*,
1211 319–321, doi:10.1038/nature07818.

1212 Willbold, M., and A. Stracke (2006), Trace element composition of mantle end-members:
1213 Implications for recycling of oceanic and upper and lower continental crust, *Geochem-*
1214 *istry, Geophysics, Geosystems*, *7*(4), 1–30, doi:10.1029/2005GC001005.

1215 Xu, Y., T. J. Shankland, S. Linhardt, D. C. Rubie, F. Langenhorst, and K. Klasinski
1216 (2004), Thermal diffusivity and conductivity of olivine, wadsleyite and ringwoodite
1217 to 20 GPa and 1373 K, *Physics of the Earth and Planetary Interiors*, *143-144*, 321–336,
1218 doi:10.1016/j.pepi.2004.03.005.

1219 Yamauchi, H., and Y. Takei (2016), Polycrystal anelasticity at near-solidus temperatures,
1220 *Journal of Geophysical Research: Solid Earth*, *121*, 1–31, doi:10.1002/2016JB013316.

1221 Zhou, Q., L. Liu, and J. Hu (2018), Western US volcanism due to intruding oceanic
1222 mantle driven by ancient Farallon slabs, *Nature Geoscience*, *11*(1), 70–76, doi:
1223 10.1038/s41561-017-0035-y.

Province	SRP avg (n=12)	GP avg (n=8)	ETZ avg (n=13)	STZ avg (n=18)	SE avg (n=5)
SiO_2 (wt%)	47.34 ± 0.78	48.84 ± 0.62	49.13 ± 1.94	46.71 ± 1.56	49.06 ± 1.44
Al_2O_3	15.43 ± 0.40	15.88 ± 0.71	15.02 ± 0.31	15.39 ± 0.58	14.36 ± 0.33
$Fe_2O_3^T$	12.62 ± 0.85	11.72 ± 0.47	12.30 ± 0.44	11.95 ± 0.86	11.71 ± 0.37
MgO	9.37 ± 0.81	8.62 ± 1.09	9.08 ± 0.86	8.79 ± 0.91	8.10 ± 0.35
CaO	10.52 ± 0.43	9.24 ± 0.26	9.10 ± 0.35	9.45 ± 1.03	9.52 ± 0.82
Na_2O	2.41 ± 0.22	3.36 ± 0.11	2.90 ± 0.27	3.16 ± 0.55	3.05 ± 0.19
K_2O	0.53 ± 0.15	0.97 ± 0.25	0.83 ± 0.39	1.11 ± 0.50	0.79 ± 0.15
TiO_2	1.74 ± 0.39	1.54 ± 0.19	1.63 ± 0.40	2.05 ± 0.34	1.77 ± 0.24
MnO	0.19 ± 0.01	0.17 ± 0.01	0.16 ± 0.02	0.18 ± 0.01	0.16 ± 0.01
P_2O_5	0.40 ± 0.08	0.41 ± 0.03	0.28 ± 0.14	0.45 ± 0.16	0.31 ± 0.06
Li (ppm)	6.99 ± 0.80	8.42 ± 1.24	6.99 ± 1.47	10.74 ± 8.56	10.54 ± 2.31
Be	0.68 ± 0.14	0.99 ± 0.23	0.93 ± 0.38	1.43 ± 0.51	0.95 ± 0.14
P	1425 ± 366	1791 ± 125	1244 ± 656	2031 ± 751	1475 ± 204
K	3574 ± 790	8893 ± 2447	6999 ± 3292	9386 ± 4040	7476 ± 1422
Sc	32.23 ± 3.26	27.85 ± 2.63	23.86 ± 1.99	25.62 ± 4.06	22.44 ± 1.44
Ti	10139 ± 2539	9470 ± 1291	9771 ± 2537	12299 ± 2351	11550 ± 1340
V	247.1 ± 14.8	191.6 ± 17.1	198.5 ± 22.5	221.2 ± 31.9	199.7 ± 7.4
Cr	391.3 ± 132.9	245.4 ± 72.3	275.3 ± 28.2	274.5 ± 57.0	296.9 ± 34.0
Mn	1447 ± 55	1379 ± 181	1396 ± 117	1487 ± 115	1355 ± 201
Co	51.70 ± 2.91	58.95 ± 6.56	77.77 ± 13.70	70.33 ± 11.59	242.2 ± 406.0
Ni	139.8 ± 46.7	156.0 ± 47.0	199.5 ± 31.6	173.7 ± 45.7	221.0 ± 39.8
Cu	52.72 ± 16.29	58.50 ± 16.03	85.15 ± 21.32	59.72 ± 11.63	96.28 ± 15.76
Zn	92.33 ± 12.10	87.84 ± 5.01	92.79 ± 4.82	81.04 ± 9.27	99.32 ± 5.11
Ga	17.15 ± 1.30	18.42 ± 0.60	18.29 ± 0.81	18.46 ± 0.67	19.80 ± 0.74
Rb	9.42 ± 3.36	14.47 ± 7.15	14.96 ± 4.66	17.11 ± 7.82	17.79 ± 2.36
Sr	239.5 ± 44.0	600.9 ± 68.5	376.0 ± 169.5	590.2 ± 188.8	368.8 ± 55.9
Y	27.91 ± 3.33	24.08 ± 1.65	21.98 ± 1.93	25.58 ± 2.18	23.54 ± 0.77
Zr	159.1 ± 32.0	155.2 ± 22.6	134.6 ± 49.3	182.6 ± 50.7	129.4 ± 15.7
Nb	16.73 ± 3.68	23.95 ± 8.29	19.70 ± 11.70	43.76 ± 17.72	25.28 ± 6.21
Sn	0.80 ± 0.17	1.06 ± 0.20	1.00 ± 0.26	1.30 ± 0.30	1.08 ± 0.23
Cs	0.10 ± 0.04	0.13 ± 0.15	0.37 ± 0.32	0.45 ± 0.59	0.12 ± 0.06
Ba	263.7 ± 50.5	410.5 ± 84.0	193.8 ± 79.5	345.7 ± 96.5	303.5 ± 67.2
La	15.53 ± 3.05	22.46 ± 2.52	15.31 ± 7.70	27.52 ± 8.61	17.44 ± 2.99
Ce	33.60 ± 6.85	45.74 ± 4.09	32.04 ± 15.20	54.16 ± 15.69	35.69 ± 5.72
Pr	4.44 ± 0.93	5.61 ± 0.39	4.04 ± 1.78	6.39 ± 1.69	4.51 ± 0.67
Nd	19.61 ± 4.12	23.04 ± 1.63	17.44 ± 6.92	26.03 ± 6.22	19.71 ± 2.71
Sm	4.69 ± 0.93	4.81 ± 0.29	4.16 ± 1.22	5.46 ± 0.98	4.83 ± 0.58
Eu	1.66 ± 0.30	1.58 ± 0.10	1.40 ± 0.35	1.81 ± 0.33	1.64 ± 0.17
Gd	5.04 ± 0.87	4.72 ± 0.21	4.36 ± 0.87	5.42 ± 0.78	5.21 ± 0.40
Tb	0.83 ± 0.13	0.74 ± 0.04	0.70 ± 0.10	0.84 ± 0.11	0.83 ± 0.05
Dy	5.08 ± 0.72	4.31 ± 0.23	4.09 ± 0.45	4.83 ± 0.50	4.68 ± 0.31
Ho	1.05 ± 0.13	0.85 ± 0.06	0.79 ± 0.07	0.92 ± 0.09	0.87 ± 0.03
Er	2.97 ± 0.32	2.38 ± 0.22	2.18 ± 0.17	2.53 ± 0.27	2.35 ± 0.13
Tm	0.43 ± 0.05	0.34 ± 0.04	0.31 ± 0.03	0.36 ± 0.04	0.32 ± 0.02
Yb	2.62 ± 0.24	2.06 ± 0.22	1.90 ± 0.17	2.21 ± 0.27	1.90 ± 0.17
Lu	0.40 ± 0.04	0.30 ± 0.04	0.28 ± 0.02	0.32 ± 0.04	0.27 ± 0.03
Hf	3.49 ± 0.69	3.08 ± 0.37	3.10 ± 0.93	4.05 ± 0.92	3.18 ± 0.34
Ta	0.94 ± 0.39	1.27 ± 0.44	1.55 ± 0.74	3.02 ± 1.41	3.10 ± 3.60
Tl	0.02 ± 0.01	0.03 ± 0.01	0.04 ± 0.01	0.03 ± 0.01	0.02 ± 0.01
Pb	2.76 ± 0.65	4.16 ± 2.29	2.80 ± 0.89	2.63 ± 1.10	1.78 ± 0.41
Th	0.98 ± 0.28	2.11 ± 0.50	1.88 ± 0.64	3.44 ± 1.46	1.90 ± 0.36
U	0.31 ± 0.12	0.44 ± 0.28	0.68 ± 0.25	0.95 ± 0.43	0.58 ± 0.14
ε_{Nd}	-5.09 ± 0.06		5.11		

Province	NBR avg (n=2)	WTZ avg (n=40)	BR avg (n=7)	RGR avg (n=65)	CP avg (n=7)
SiO_2 (wt%)	47.01 ± 0.24	46.36 ± 1.89	46.13 ± 1.46	45.24 ± 1.13	41.37 ± 1.21
Al_2O_3	16.76 ± 0.39	14.18 ± 1.06	15.21 ± 0.59	14.89 ± 0.63	11.07 ± 0.52
$Fe_2O_3^T$	11.88 ± 0.18	12.15 ± 0.91	12.85 ± 1.17	11.68 ± 0.57	13.39 ± 0.61
MgO	7.40 ± 0.29	9.98 ± 1.47	8.28 ± 0.90	9.88 ± 1.23	9.28 ± 1.44
CaO	9.51 ± 0.04	9.90 ± 1.00	9.29 ± 0.41	10.29 ± 0.63	11.26 ± 0.46
Na_2O	3.25 ± 0.00	3.22 ± 0.48	3.60 ± 0.38	3.48 ± 0.48	3.60 ± 0.76
K_2O	1.12 ± 0.15	1.24 ± 0.44	1.50 ± 0.50	1.60 ± 0.39	0.86 ± 0.28
TiO_2	2.15 ± 0.04	2.06 ± 0.53	2.53 ± 0.35	2.31 ± 0.17	3.72 ± 0.22
MnO	0.19 ± 0.01	0.18 ± 0.01	0.19 ± 0.01	0.18 ± 0.01	0.19 ± 0.02
P_2O_5	0.54 ± 0.04	0.60 ± 0.19	0.55 ± 0.13	0.54 ± 0.08	1.45 ± 0.44
Li (ppm)	11.63 ± 2.98	9.98 ± 3.66	8.31 ± 2.00	8.33 ± 1.70	32.66 ± 14.02
Be	1.28 ± 0.06	1.63 ± 0.56	1.47 ± 0.52	1.61 ± 0.15	2.77 ± 0.85
P	2303 ± 118	2655 ± 942	2517 ± 567	2378 ± 253	6393 ± 2118
K	8737 ± 1209	9326 ± 3495	12970 ± 4787	13815 ± 2265	7126 ± 2262
Sc	29.05 ± 1.34	23.55 ± 4.32	21.14 ± 2.43	29.09 ± 3.47	18.10 ± 2.88
Ti	12603 ± 229	8048 ± 4786	15469 ± 2246	14099 ± 1691	21706 ± 1529
V	251.2 ± 34.1	222.4 ± 25.0	218.9 ± 12.6	222.7 ± 23.2	244.6 ± 28.4
Cr	164.2 ± 63.2	360.0 ± 148.3	213.8 ± 85.2	283.0 ± 78.6	233.8 ± 81.9
Mn	1496 ± 57	1395 ± 138	1496 ± 88	1531 ± 150	1576 ± 122
Co	39.64 ± 0.25	57.14 ± 17.00	58.37 ± 8.70	63.41 ± 6.84	52.36 ± 5.51
Ni	115.3 ± 32.2	206.9 ± 51.5	138.8 ± 36.9	183.4 ± 49.7	190.8 ± 64.8
Cu	51.25 ± 2.05	61.40 ± 11.09	40.33 ± 4.24	53.09 ± 2.93	53.99 ± 9.90
Zn	77.15 ± 0.07	100.3 ± 14.7	89.73 ± 6.43	76.68 ± 5.84	138.9 ± 23.6
Ga	17.47 ± 0.12	17.77 ± 3.31	19.64 ± 1.22	19.47 ± 1.06	22.36 ± 2.03
Rb	21.06 ± 0.59	20.03 ± 7.92	36.47 ± 15.40	33.72 ± 9.57	13.92 ± 7.22
Sr	365.7 ± 30.1	752.0 ± 236.1	644.8 ± 96.3	652.1 ± 94.7	1654 ± 482
Y	37.00 ± 0.42	23.59 ± 2.08	28.86 ± 1.77	27.71 ± 2.33	37.87 ± 8.92
Zr	206.2 ± 22.3	195.8 ± 57.6	227.1 ± 76.1	192.3 ± 28.4	532.0 ± 153.1
Nb	41.10 ± 5.94	50.13 ± 21.21	55.16 ± 19.70	57.11 ± 9.20	119.6 ± 31.9
Sn	1.34 ± 0.05	1.32 ± 0.34	1.43 ± 0.44	1.33 ± 0.13	2.69 ± 0.46
Cs	0.25 ± 0.14	1.41 ± 5.88	0.30 ± 0.17	0.30 ± 0.11	1.34 ± 1.38
Ba	292.2 ± 62.2	648.7 ± 290.5	387.4 ± 54.9	490.0 ± 87.2	1070 ± 137
La	21.14 ± 1.39	42.01 ± 17.03	32.00 ± 10.39	36.40 ± 6.03	104.5 ± 34.1
Ce	46.84 ± 2.40	80.88 ± 29.95	64.82 ± 19.44	69.28 ± 10.28	215.0 ± 68.7
Pr	6.20 ± 0.20	9.47 ± 3.23	7.90 ± 2.03	8.72 ± 1.24	25.57 ± 8.00
Nd	27.07 ± 0.30	36.55 ± 11.60	32.80 ± 7.33	34.85 ± 4.27	102.1 ± 30.4
Sm	6.10 ± 0.16	6.86 ± 1.72	6.81 ± 1.16	6.90 ± 0.63	17.63 ± 4.51
Eu	2.03 ± 0.06	2.11 ± 0.46	2.26 ± 0.35	2.20 ± 0.18	5.08 ± 1.29
Gd	6.38 ± 0.16	6.05 ± 1.12	6.54 ± 0.76	6.46 ± 0.44	13.51 ± 2.84
Tb	1.04 ± 0.03	0.88 ± 0.14	1.00 ± 0.10	0.97 ± 0.06	1.73 ± 0.40
Dy	6.35 ± 0.23	4.67 ± 0.56	5.52 ± 0.39	5.32 ± 0.31	8.34 ± 1.77
Ho	1.33 ± 0.04	0.86 ± 0.08	1.03 ± 0.07	1.02 ± 0.06	1.37 ± 0.30
Er	3.80 ± 0.12	2.19 ± 0.24	2.82 ± 0.16	2.62 ± 0.17	3.23 ± 0.66
Tm	0.56 ± 0.01	0.30 ± 0.03	0.39 ± 0.03	0.40 ± 0.03	0.40 ± 0.08
Yb	3.50 ± 0.11	1.78 ± 0.27	2.33 ± 0.11	2.36 ± 0.17	2.23 ± 0.46
Lu	0.54 ± 0.01	0.26 ± 0.04	0.34 ± 0.02	0.37 ± 0.03	0.29 ± 0.06
Hf	4.58 ± 0.27	4.49 ± 1.22	4.90 ± 1.31	4.68 ± 0.60	10.85 ± 2.66
Ta	2.19 ± 0.30	2.89 ± 1.18	3.21 ± 1.14	3.86 ± 0.72	6.44 ± 1.54
Tl	0.02 ± 0.01	0.04 ± 0.02	0.03 ± 0.01	0.03 ± 0.01	0.07 ± 0.06
Pb	1.64 ± 0.33	5.88 ± 2.16	1.91 ± 0.68	1.88 ± 0.76	7.17 ± 2.32
Th	1.90 ± 0.03	6.12 ± 2.92	3.62 ± 1.81	4.34 ± 0.88	11.60 ± 3.45
U	0.63 ± 0.06	1.69 ± 0.76	1.02 ± 0.48	1.18 ± 0.26	3.75 ± 1.96
ε_{Nd}		2.38		6.04 0.49	

Table 1. Average compositions used for inverse modeling. Major elements are reported as oxide wt%, trace elements as ppm. SRP = Snake River Plain; GP = Great Plains; ETZ = Eastern Transition Zone; STZ = Southern Transition Zone; SE = Sentinel Plain; NBR = Northern Basin and Range; WTZ = Western Transition Zone; BR = Basin and Range; RGR = Rio Grande Rift; CP = Colorado Plateau. Samples from SRP include L73-64 and L73-112 from *Leeman et al.* [2009] and I-2725 from *White et al.* [2004]. Samples from WTZ include AZ-09 UK-1, 2, 11, 13b, 18, 19b, 22, 23b, 26, 27, 30, 31b, 32–35, SC 07 03, and SC 07 05 generously provided by T. Plank [written communication, 2015; *Plank and Forsyth*, 2016]. Samples from RGR include 671, 672, 674–676, 678, 695, 699, 860, 864–866, 869, 870, 875, 879, 882, 883, 888, 894, 895, 898, 6100, 6102–6104, 6108, 6110, 6130, 6140, 6143, 6151, 6152, 6155, 6157, 6158, 6185, 6187, 8101, 8103, 8107, 8109–8112, 8128, 8129, 8134, 8136, 8138–8140, 8144, 8157, 8159–8161, and 8164 from *Thompson et al.* [2005].

Table 2. Summary of REE inverse modeling for 26 volcanic fields from ten geographic provinces. F = cumulative melt fraction; T_P = potential temperature; SRP = Snake River Plain; GP = Great Plains; ETZ = Eastern Transition Zone; STZ = Southern Transition Zone; SE = Sentinel Plain; NBR = Northern Basin and Range; WTZ = Western Transition Zone; BR = Basin and Range; RGR = Rio Grande Rift; CP = Colorado Plateau; A = Albuquerque; E = eastern SRP; G = Geronimo; GC = Grand Canyon; HB = Hopi Buttes; J = Jornado del Muerto; L = Lucero; LC = Lunar Crater; M = Mormon Mountain; MD = Mojave Desert; MR = Magic Reservoir; MT = Mount Taylor; N-E = north-eastern SRP; NN = Northern Nevada; O = Ocate; P = Potrillo; RC = Raton-Clayton; SC = San Carlos; S-E = south-eastern SRP; SF = San Francisco; SP = Springerville; Y = Yellowstone; W-C = west-central SRP; WP = Washington-Panguitch; ZB = Zuni-Bandera. T_P WUSA16 refers to potential temperature calculated from shear wave velocity at 75 km depth.

Province	Field	Age Ma	Latitude °N	Longitude °W	Depth km	F	T_P °C	T_P WUSA16 °C
SRP	E	6.51	43.50	-113.00	48–80	0.10	1354–1376	1372
	MR	9	43.00	-114.20				1371
	N-E	5	43.57	-112.05				1366
	S-E	7	42.94	-111.33				1333
	W-C	13	43.10	-115.73				1350
	Y	1	44.00	-110.50				1356
GP	O	3	36.03	-104.93	53–83	0.07	1355–1361	1341
	RC	2.9	36.78	-103.84				1329
ETZ	A	0.2	34.83	-106.90	57–77	0.06	1345–1357	1350
	L	1.3	34.95	-107.21				1347
	MT	2	35.00	-108.50				1328
	ZB	0.5	34.99	-108.26				1333
STZ	SC	1	33.34	-110.39	54–79	0.06	1350–1352	1337
	SP	2	34.10	-109.59				1335
	G	0.26	31.00	-109.30				1321
SE	SE	3	33.05	-113.02	53–78	0.06	1347–1354	1311
NBR	NN	4.5	40.51	-117.12	54–69	0.04	1328–1331	1342
WTZ	GC	1	36.34	-113.10	62–72	0.02	1327–1328	1335
	M	14	34.65	-111.64				1330
	SF	1	35.43	-112.05				1335
	WP	1	37.23	-113.35				1336
BR	LC	4.65	38.47	-115.95	60–70	0.02	1322–1326	1337
	MD	2.7	34.91	-115.90				1330
RGR	J	1	33.41	-107.05	59–72	0.02	1321–1322	1344
	P	0.2	31.97	-107.16				1343
CP	HB	2.1	35.38	-110.25	62–72	0.01	1318–1322	1318

Figure 1. (**a**) Topographic map of western North America where colored circles show spatial and temporal distribution of mafic volcanism (sample locations with MgO >4 wt% are colored by age and taken from NAVDAT database. Arrow = velocity of North American plate with respect to Pacific plate [26.8 $\pm$ 7.8 mm yr^{-1}; *Gripp and Gordon*, 2002]; Y = Yellowstone. (**b**) Long wavelength (500–4000 km) free-air gravity anomalies [*Bruinsma et al.*, 2014]. Mafic volcanism as before. (**c**) Map showing shear wave velocities at 100 km depth from SL2013NA tomographic model [*Schaeffer and Lebedev*, 2014]. Mafic volcanism as before.

Figure 2. Locations of samples used in study. Small black circles = Cenozoic mafic samples from NAVDAT database; red circles = screened samples from Snake River Plain (SRP); pink hexagons = samples from Great Plains (GP); orange stars = samples from Eastern Transition Zone (ETZ); light green right-pointing triangles = samples from Southern Transition Zone (STZ); light blue diamonds = samples from Sentinel Plain (SE); turquoise squares = samples from Northern Basin and Range (NBR); green inverted triangles = samples from Western Transition Zone (WTZ); blue squares = samples from Basin and Range; dark green triangles = samples from Rio Grande Rift (RGR); dark blue stars = samples from Colorado Plateau; gray circles = samples excluded due to suspected lithospheric contamination; black lines = physiographic regions [*Thompson and Zoback*, 1979]; Y = Yellowstone. Database includes 77 samples from *White et al.* [2004], *Thompson et al.* [2005], *Leeman et al.* [2009], and *Plank and Forsyth* [2016] together with 100 new samples.

Figure 3. Selection criteria for most primitive (i.e. asthenospheric) samples. (**a**) SiO_2 concentrations plotted as function of MgO. Small black circles = Cenozoic samples from NAVDAT database; red circles = samples from Snake River Plain (SRP); pink hexagons = samples from Great Plains (GP); orange stars = samples from Eastern Transition Zone (ETZ); light green right-pointing triangles = samples from Southern Transition Zone (STZ); light blue diamonds = samples from Sentinel Plain (SE); turquoise squares = samples from Northern Basin and Range (NBR); green inverted triangles = samples from Western Transition Zone (WTZ); blue squares = samples from Basin and Range; dark green triangles = samples from Rio Grande Rift (RGR); dark blue stars = samples from Colorado Plateau (CP); gray circles = samples excluded after applying selection criteria; dashed line = sample cut-off at MgO <7 wt% to exclude highly fractionated samples (note that higher cut-off of 8 wt% was used for SRP and STZ samples). (**b**) CaO concentrations plotted as function of MgO. Symbols and dashed line as before. (**c**) $Fe_2O_3^T$ (i.e. total Fe expressed as Fe_2O_3) concentrations plotted as function of MgO. Symbols and dashed line as before. (**d**) La/Ba ratios plotted as function of La/Nb ratios. Symbols as before. Dashed ellipse = delineation of range of ratios for Ocean Island Basalts [samples outside of ellipse deemed to be affected by lithospheric and/or subduction fluid contamination; *Fitton et al.*, 1991; *Stracke et al.*, 2003].

Figure 4. (**a**) Averaged trace element distribution of basaltic samples from Snake River Plain (SRP) chosen in accordance with selection criteria (Figure 3). Compositions normalized to primitive mantle [*McDonough and Sun*, 1995]. Red line with gray band = mean values for province $\pm 1\sigma$; pair of dashed lines = range of compositions from all provinces; (**b-l**) Averaged trace element distributions for Great Plains (GP), Eastern Transition Zone (ETZ), Southern Transition Zone (STZ), Sentinel Plain (SE), Northern Basin and Range (NBR), Western Transition Zone (WTZ), Basin and Range (BR), Rio Grande Rift (RGR), and Colorado Plateau (CP).

Figure 5. Inverse modeling of screened samples. (**a**) Rare earth element (REE) concentrations for samples from Snake River Plain (SRP) normalized to primitive mantle [*McDonough and Sun*, 1995]. Red circles with vertical bars = average concentrations $\pm 1\sigma$; red line = best-fit concentrations calculated by inverse modeling. (**b**) Trace element concentrations for SRP. Red circles with vertical bars = average concentrations $\pm 1\sigma$; red line = concentrations predicted by forward modeling. (**c**) Melt fraction as function of depth. Red line = melt fraction corrected for olivine fractionation obtained by fitting average REE concentrations shown in panel (**a**); dashed line = same but uncorrected for olivine fractionation; solid black lines = isentropic curves calculated using parameterization from *Katz et al.* [2003] and labeled according to potential temperature; vertical dashed lines = phase transitions for spinel and garnet. Inset panel summarizes: (i) source composition where PM = primitive mantle; (ii) average wt % of MgO plus its uncertainty; (iii) percentage of olivine fractionation; and (iv) total melt thickness. (**d-f**) Great Plains (GP). Inset panel as before where source composition is now given as percentages of Depleted MORB Mantle (DMM) and Primitive Mantle (PM) estimated from ε_{Nd} values (Table 1). (**g-k**) Eastern Transition Zone (ETZ). (**l-n**) Southern Transition Zone (STZ). (**o-q**) Sentinel Plain (SE).

Figure 6. Inverse modeling of screened samples. (**a**) Rare earth element (REE) concentrations for samples from Northern Basin and Range (NBR) normalized to primitive mantle [*McDonough and Sun*, 1995]. Turquoise squares with vertical bars = average concentrations $\pm 1\sigma$; turquoise line = best-fit concentrations calculated by inverse modeling. (**b**) Trace element concentrations for NBR. Turquoise squares with vertical bars = average concentrations $\pm 1\sigma$; turquoise line = concentrations predicted by forward modeling. (**c**) Melt fraction as function of depth. Turquoise line = melt fraction corrected for olivine fractionation obtained by fitting average REE concentrations shown in panel (**a**); dashed line = same but uncorrected for olivine fractionation; solid black lines = isentropic curves calculated using parameterization from *Katz et al.* [2003] and labeled according to potential temperature; vertical dashed lines = phase transitions for spinel and garnet. Inset panel summarizes: (i) source composition given as percentages of Depleted MORB Mantle (DMM) and Primitive Mantle (PM) estimated from ε_{Nd} values (Table 1); (ii) average wt % of MgO plus its uncertainty; (iii) percentage of olivine fractionation; (iv) total melt thickness. (**d-f**) Western Transition Zone (WTZ). (**g-k**) Basin and Range (BR). (**l-n**) Rio Grande Rift (RGR). (**o-q**) Colorado Plateau (CP). Inset panel as before but source composition is now Depleted MORB Mantle (DMM) with 20% enrichment by small fraction melt generated within garnet stability field.

Figure 7. (**a**) Map of shear wave velocity at depth of 75 km from PM2012 tomographic model [*Priestley and M^{c}Kenzie*, 2013]. Small black circles = Cenozoic mafic samples from NAVDAT database; large black circles = basaltic samples analyzed in this study; thin black lines = physiographic regions (Figure 2); Colored squares = loci of velocity profiles shown in Figure 8. (**b**) Same for SL2013NA tomographic model [*Schaeffer and Lebedev*, 2014]. (**c**) Same for DNA13 model [*Porritt et al.*, 2014]. (**d**) Same for WUSA16 model [*Shen and Ritzwoller*, 2016].

Figure 8. Shear wave velocity and temperature profiles. (**a**) Shear wave velocity, V_s, as function of depth for ten locations shown on Figure 7a with same color scheme [PM2012 tomographic model; *Priestley and M^{c}Kenzie*, 2013]. Red line = Snake River Plain (SRP); pink line = Great Plains (GP); orange line = Eastern Transition Zone (ETZ); light green line = Southern Transition Zone (STZ); light blue line = Sentinel Plain (SE); turquoise line = Northern Basin and Range (NBR); green line = Western Transition Zone (WTZ); blue line = Basin and Range (BR); dark green line = Rio Grande Rift (RGR); dark blue line = Colorado Plateau (CP); coarse dashed line = Western United States (WUS) reference velocity model [*Pollitz*, 2008]. (**b**) Temperature as function of depth calculated from V_s profiles shown in panel (**a**). Colored scheme as before. Dashed lines = isentropic curves labeled according to potential temperature, T_p; horizontal line = maximum crustal thickness of 50 km [*Shen and Ritzwoller*, 2016]; solid diagonal line = solidus for dry mantle peridotite [*Katz et al.*, 2003]. (**c-d**) Same for SL2013NA tomographic model [*Schaeffer and Lebedev*, 2014]. (**e-f**) Same for DNA13 [*Porritt et al.*, 2014]. (**g-h**) Same for WUSA16 [*Shen and Ritzwoller*, 2016].

Figure 9. (**a**) Map of lithospheric thickness calculated from $V_s(z)$ profiles for PM2012 tomographic model [*Priestley and M^{c}Kenzie*, 2013]. Black circles = volcanic activity younger than 10 Ma (NAVDAT). (**b**) Map of potential temperature calculated from V_s values at 75 km depth for PM2012 model. (**c-d**) Same for SL2013NA [*Schaeffer and Lebedev*, 2014]. (**e-f**) Same for DNA13 [*Porritt et al.*, 2014]. (**g-h**) Same for WUSA16 [*Shen and Ritzwoller*, 2016].

Figure 10. Tomographic and geochemical temperatures. (**a**) Shear wave velocity, V_s, plotted as function of La/Yb ratio for 177 individual samples (see Figure 2 for locations). Each value of V_s is averaged over 0.5° radius around each volcanic center at depth of 75 km, except for samples from CP, G (STZ) and SE from PM2012 model that are averaged over 1.2° radius [*Priestley and M^{c}Kenzie*, 2013]. Note that V_s values $>$4.218 km/s were excised before averaging to mitigate effect of fast cratonic roots where no melting is expected to have occurred. Red circles = Snake River Plain (SRP); pink hexagons = Great Plains (GP); orange stars = Eastern Transition Zone (ETZ); light green right-pointing triangles = Southern Transition Zone (STZ); light blue diamonds = Sentinel Plain (SE); turquoise squares = Northern Basin and Range (NBR); green inverted triangles = Western Transition Zone (WTZ); blue squares = Basin and Range; dark green triangles = Rio Grande Rift (RGR); dark blue stars = Colorado Plateau. (**b**) Potential temperatures calculated from V_s anomalies at 75 km depth plotted as function of potential temperature calculated from geochemical inverse modeling of rare earth element distributions. Colored symbols as in panel (**a**); horizontal and vertical error bars = cumulative uncertainties for calculated potential temperatures; dotted line = 1:1 relationship for visual guidance. (**c-d**) Same for SL2013NA [*Schaeffer and Lebedev*, 2014]. (**e-f**) Same for DNA13 [*Porritt et al.*, 2014]. (**g-h**) Same for WUSA16 [*Shen and Ritzwoller*, 2016].

Figure 11. (**a**) Horizontal slice at 100 km through SL2013NA tomographic model [*Schaeffer and Lebedev*, 2014]; small colored circles = heat flow measurements [*Pollack et al.*, 1993]; large colored circles = locations of $V_s(z)$ profiles for each volcanic province shown in Figure 7 where red = Snake River Plain (SRP); pink = Great Plains (GP); orange = Eastern Transition Zone (ETZ); light green = Southern Transition Zone (STZ); light blue = Sentinel Plain (SE); turquoise = Northern Basin and Range (NBR); green = Western Transition Zone (WTZ); blue = Basin and Range (BR); dark green = Rio Grande Rift (RGR); dark blue = Colorado Plateau (CP); black line labeled ***x***–***x***′ = location of transect shown in panels (**b-d**). (**b**) Vertical slice through SL2013NA model along transect shown in panel (**a**). Black line with gray band = topographic profile and crustal thickness profile from *Shen and Ritzwoller* [2016]; dashed line = putative lithosphere-asthenosphere boundary for western North America and craton from *Hopper et al.* [2018] and *Priestley and M^{c}Kenzie* [2013], respectively; colored circles = lithospheric thickness estimates from REE inverse modeling. (**c**) Gray line and band = observed regional elevation $\pm 1\sigma$ within ± 10 km corridor along transect shown in panel (**a**); dashed and pair of dotted lines = uplift $\pm 1\sigma$ calculated from shear wave velocity structure and lithosphere-asthenosphere boundary from *Hopper et al.* [2018] and *Priestley and M^{c}Kenzie* [2013]; red dashed line = uplift calculated from temperature anomaly alone; colored circles = uplift $\pm 1\sigma$ calculated using results of REE inverse modeling at locations shown in (**a**). (**d**) Gray line and small colored circles = averaged and spot heat flow measurements within ± 100 km corridor along same transect; dashed and pair of dotted lines = heat flow $\pm 1\sigma$ calculated from shear wave velocity structure and lithosphere-asthenosphere boundary from *Hopper et al.* [2018] and *Priestley and M^{c}Kenzie* [2013]; large colored circles = heat flow $\pm 1\sigma$ calculated using results of REE inverse modeling at locations shown in panel (**a**).

A: Analytic Procedures

65 samples from Arizona and Colorado were analyzed by X-ray fluorescence (XRF) on a Panalytical PW2404 wavelength-dispersive sequential X-ray spectrometer at the School of GeoSciences, University of Edinburgh. Method of analysis and estimates of precision are described in *Fitton et al.* [1998]. 280 samples were analyzed for trace elements on a PerkinElmer SCIEX Elan DRC II quadrupole ICP-MS Inductively Coupled Plasma-Mass Spectrometer (ICP-MS) at the Department of Earth Sciences, University of Cambridge. The method of analysis is similar to that used by *Eggins et al.* [1997], based upon the use of international rock standards for matrix-matched calibration. The ICP-MS internal standards were 10 ppb Rh, In and Re and each sample was diluted 5000 times for analysis in 1% HNO_3. Under the conditions used, instrumental drift was less than 5% measured for the internal standard intensity during the entire analytical run (40 or more solutions per batch). Solutions were analyzed using a Micromist nebulizer (FM05, Glass Expansion, Australia) and a quartz cyclonic baffled spray chamber with platinum sampler and skimmer cones. ICP-MS sensitivity for this configuration was 5×10^4 cps/ppb In with CeO/Ce ratios = 2%. Appropriate corrections were made using oxide/metal correction factors calculated by analyzing pure single-element standard solutions. Instrument calibration was carried out using values from the GEOREM database (version 9, 2009; `http://georem.mpch-mainz.gwdg.de`) by analyzing matrix-matched United States Geologic Survey (USGS) rock standards BIR-1, AGV-1, BHVO-2, and BCR-2, which were dissolved using the same procedures as for samples. Concentrations were calculated on a spreadsheet where raw intensities were blank subtracted, internal standard normalized, and rare earth oxide corrected. The calibration method was a simple linear calibration curve fitted to calculated slopes and the intercept was set at zero. All results (i.e. standards, unknowns) were accurately corrected for dilution by mass. Each sample was prepared by digesting 0.1 g of finely ground rock powder using 4 ml HF plus 1 ml HNO_3 in a sealed PFA vial. The acids used for sample preparation were ppb grade, which were further distilled in-house using Teflon or quartz stills. An Evapoclean (Analab, France) system consisting of a temperature-controlled Teflon-covered graphite block was used for digestions and evaporations within a closed, clean PFA environment thus avoiding the need for sample preparation to be carried out in a clean laboratory. Blanks and standards were prepared with each set of samples to monitor the quality of the sample preparation method. Total procedural blanks for all elements were very low, slightly higher than the ultra pure 1% HNO_3 rinse solution but negligible compared to sample intensities. External reproducibility, based on replicate analysis of standards and samples within batches,

1403 is 2–5% for all analytes. Accuracy for the analysis of rock standards such as BCR-2 during
1404 the run for most elements was within ∼2% of the GEOREM-preferred values and better than
1405 5% (n=5) for the rest of the elements studied.

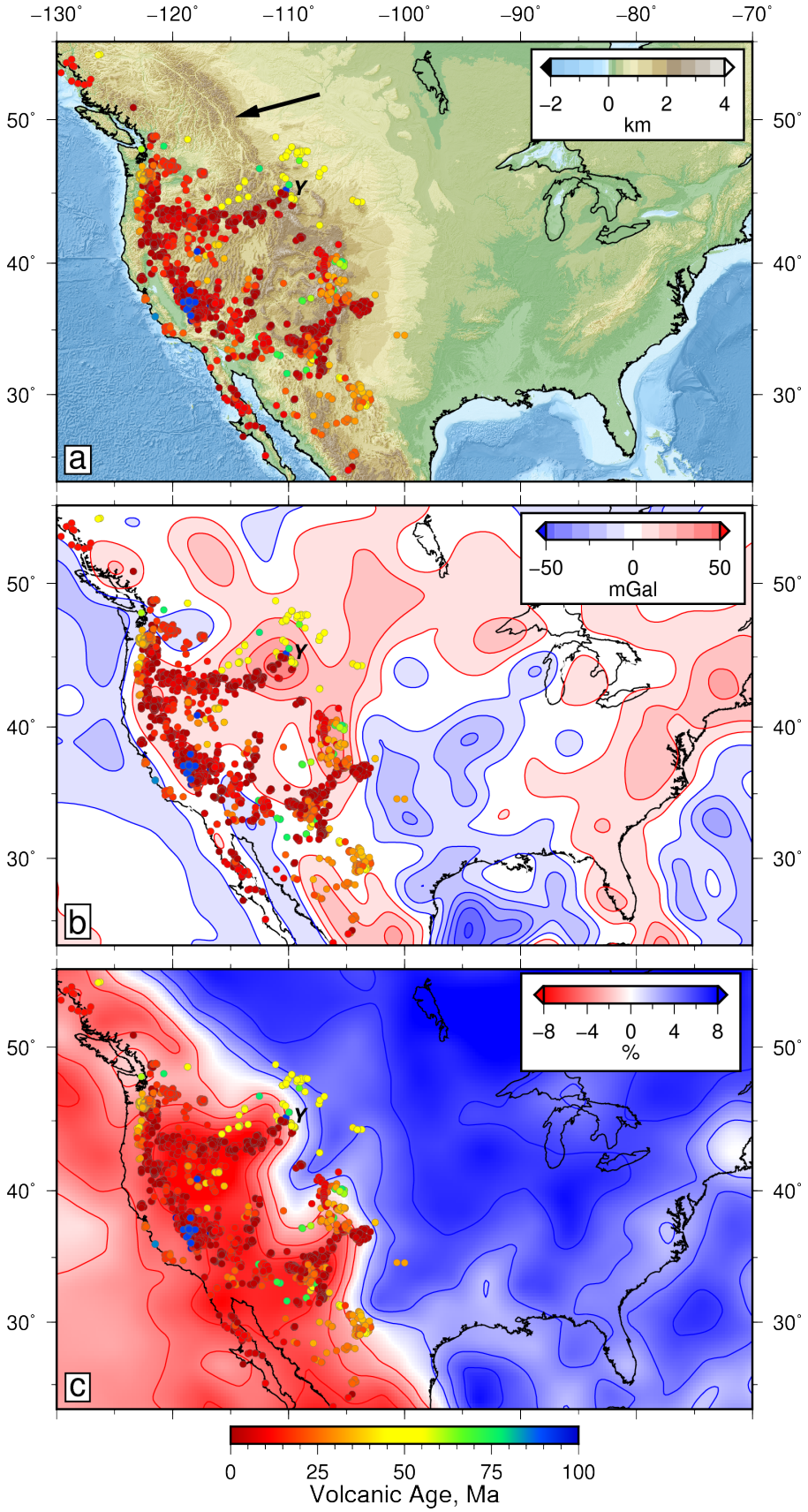
−130°
−120°
−110°
−100°
−90°
−80°
−70°
50°
40°
30°
−2
0
2
4
km
Y
a
−50
0
50
mGal
b
−8
−4
0
4
8
%
c
0
25
50
75
100
Volcanic Age, Ma

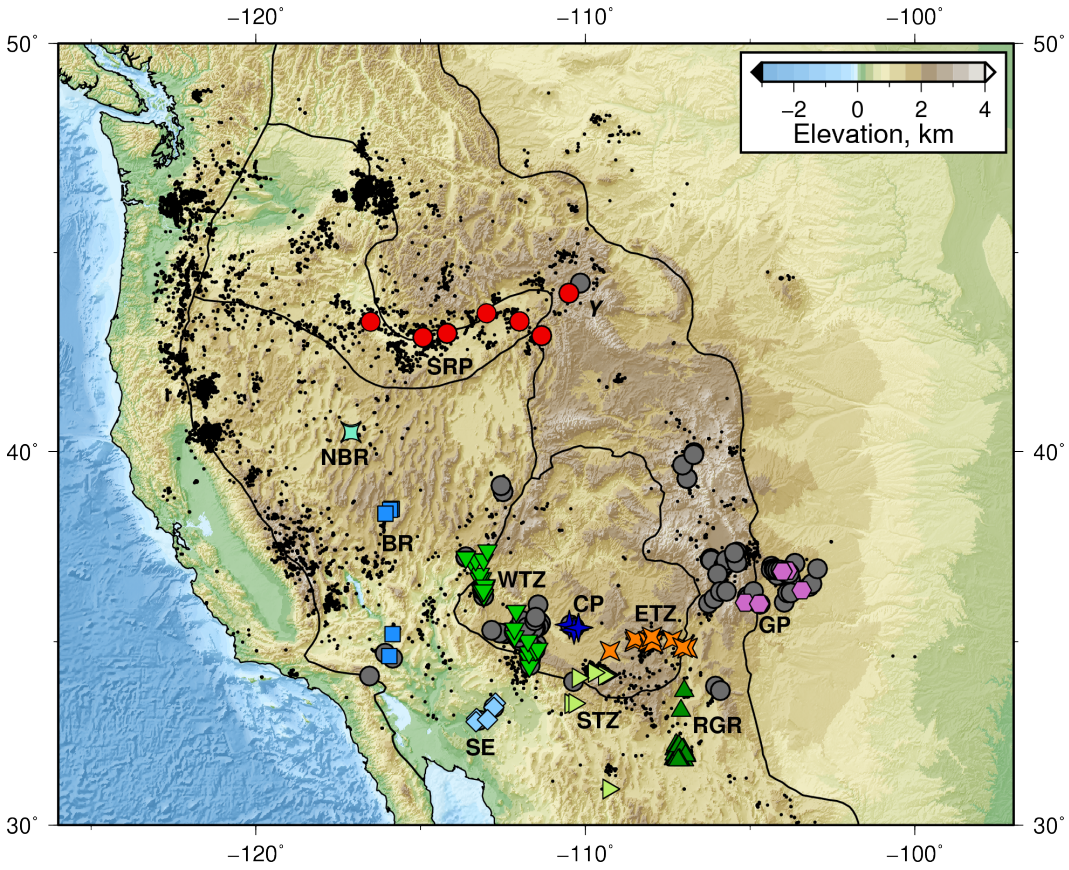
−120°
−110°
−100°
50°
40°
30°
−2
0
2
4
Elevation, km
Y
SRP
NBR
BR
WTZ
CP
ETZ
GP
STZ
RGR
SE

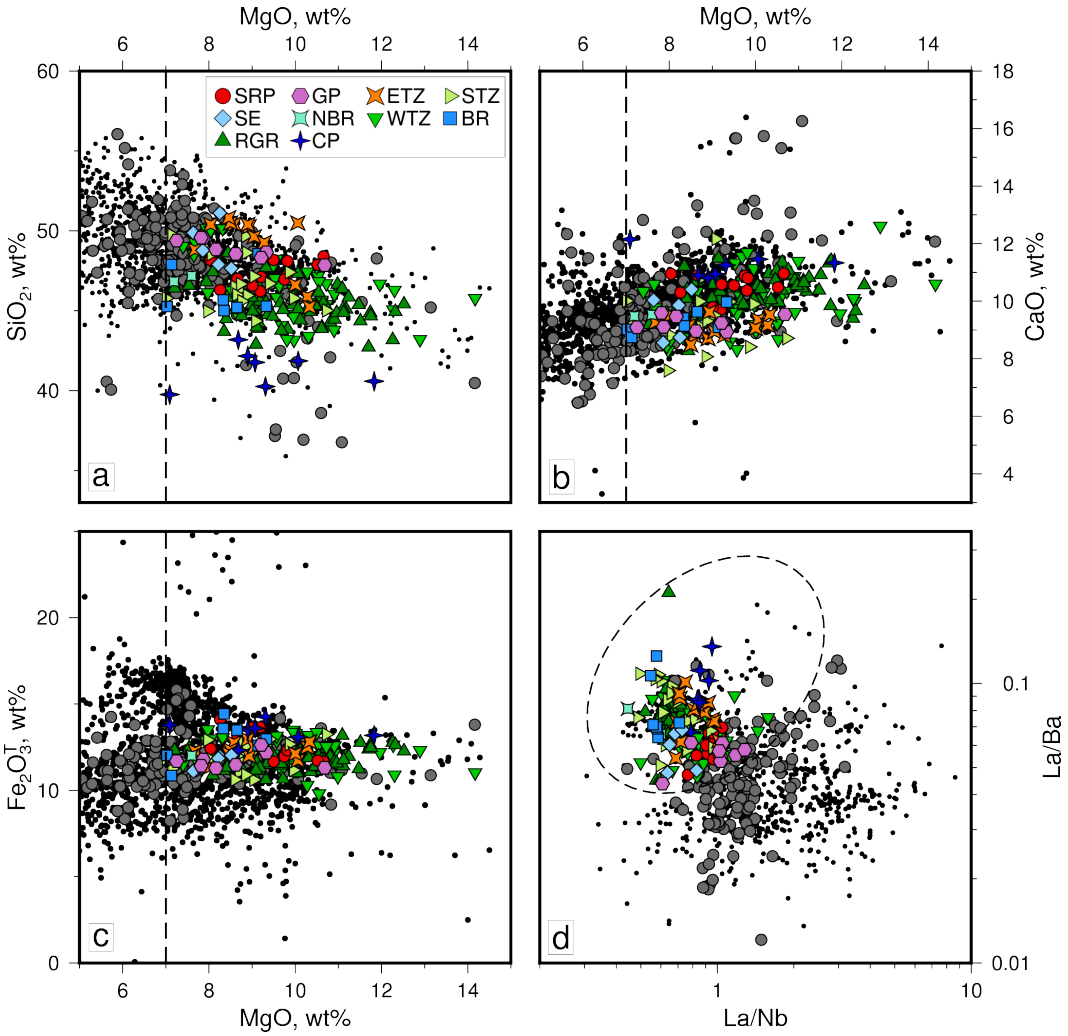
MgO, wt%
6
8
10
12
14
SRP
GP
ETZ
STZ
SE
NBR
WTZ
BR
RGR
CP
60
50
40
SiO2, wt%
a
18
16
14
12
10
8
6
4
CaO, wt%
b
20
10
0
Fe2O3T, wt%
c
0.1
0.01
La/Ba
d
1
10
La/Nb

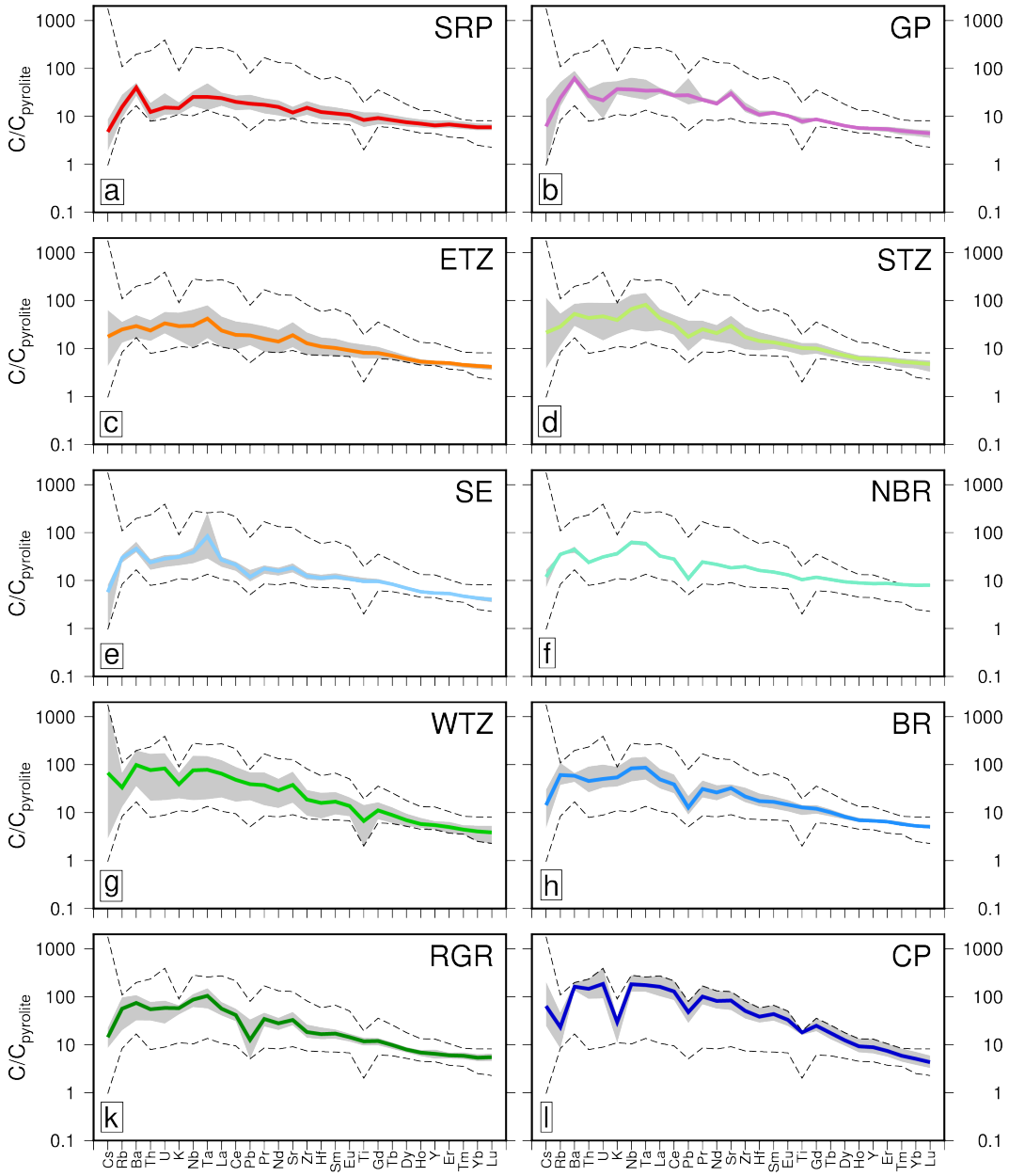
SRP
GP
ETZ
STZ
SE
NBR
WTZ
BR
RGR
CP
a
b
c
d
e
f
g
h
k
l
C/C_pyrolite
1000
100
10
1
0.1
Cs Rb Ba Th U K Nb Ta La Ce Pb Pr Nd Sr Zr Hf Sm Eu Ti Gd Tb Dy Ho Y Er Tm Yb Lu

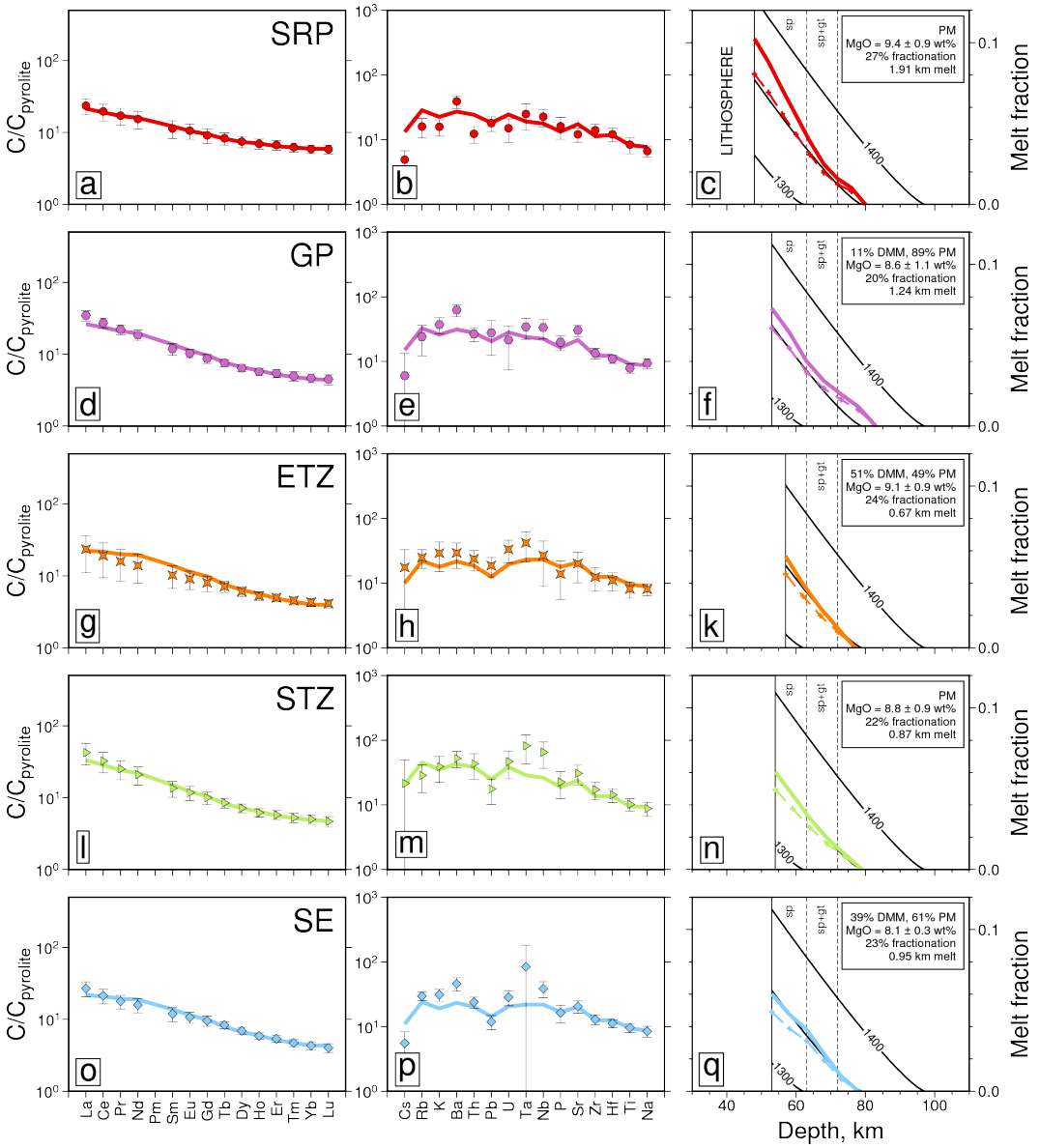
SRP
GP
ETZ
STZ
SE
a
b
c
d
e
f
g
h
k
l
m
n
o
p
q
C/C$_{pyrolite}$
LITHOSPHERE
sp
sp+gt
1400
1300
PM
MgO = 9.4 ± 0.9 wt%
27% fractionation
1.91 km melt
11% DMM, 89% PM
MgO = 8.6 ± 1.1 wt%
20% fractionation
1.24 km melt
51% DMM, 49% PM
MgO = 9.1 ± 0.9 wt%
24% fractionation
0.67 km melt
PM
MgO = 8.8 ± 0.9 wt%
22% fractionation
0.87 km melt
39% DMM, 61% PM
MgO = 8.1 ± 0.3 wt%
23% fractionation
0.95 km melt
Melt fraction
La Ce Pr Nd Pm Sm Eu Gd Tb Dy Ho Er Tm Yb Lu
Cs Rb K Ba Th Pb U Ta Nb P Sr Zr Hf Ti Na
Depth, km

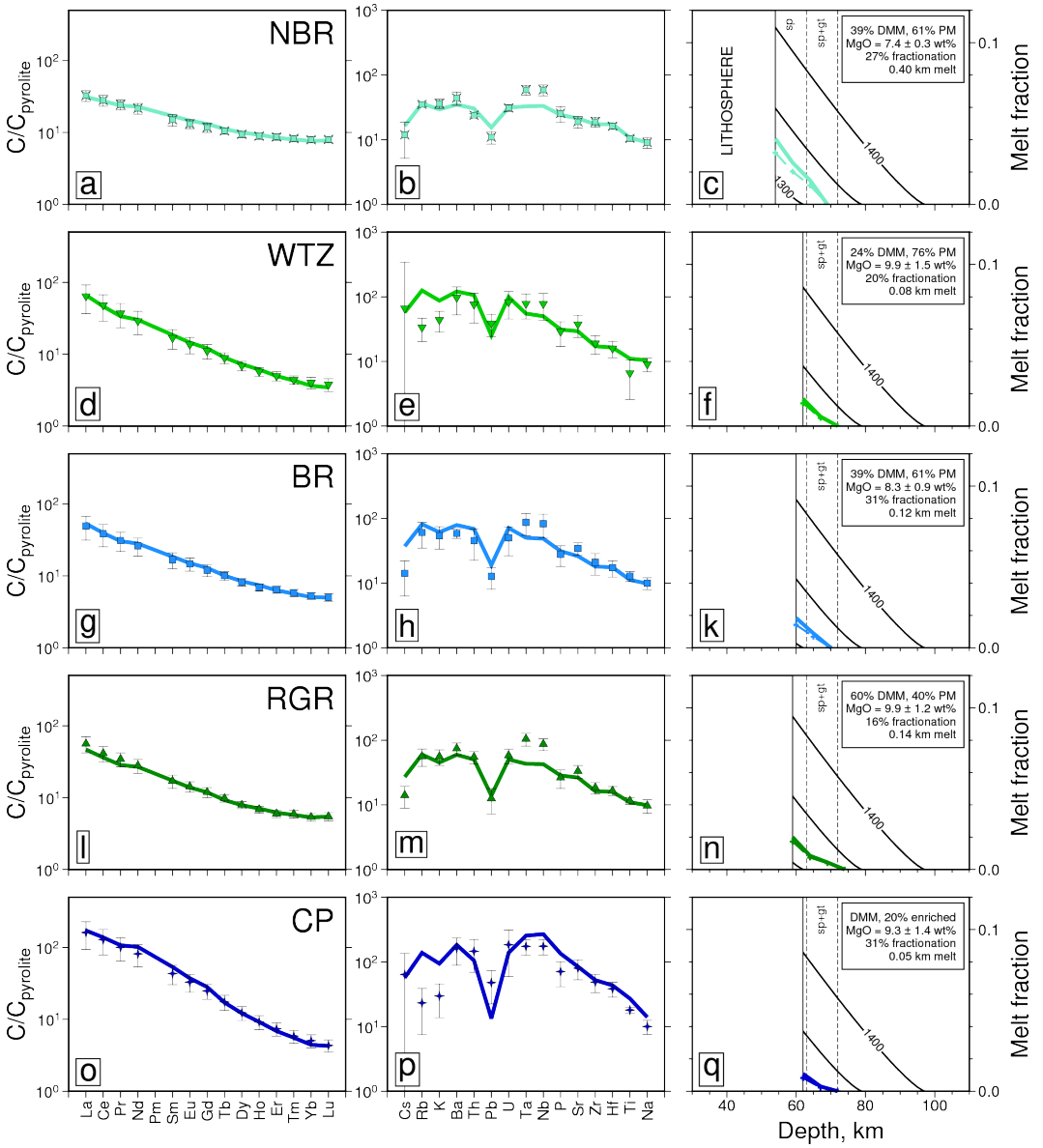
NBR
WTZ
BR
RGR
CP
a
b
c
d
e
f
g
h
k
l
m
n
o
p
q
C/C$_{pyrolite}$
Melt fraction
LITHOSPHERE
sp
sp+gt
1400
1300
39% DMM, 61% PM
MgO = 7.4 ± 0.3 wt%
27% fractionation
0.40 km melt
24% DMM, 76% PM
MgO = 9.9 ± 1.5 wt%
20% fractionation
0.08 km melt
39% DMM, 61% PM
MgO = 8.3 ± 0.9 wt%
31% fractionation
0.12 km melt
60% DMM, 40% PM
MgO = 9.9 ± 1.2 wt%
16% fractionation
0.14 km melt
DMM, 20% enriched
MgO = 9.3 ± 1.4 wt%
31% fractionation
0.05 km melt
La Ce Pr Nd Pm Sm Eu Gd Tb Dy Ho Er Tm Yb Lu
Cs Rb K Ba Th Pb U Ta Nb P Sr Zr Hf Ti Na
Depth, km

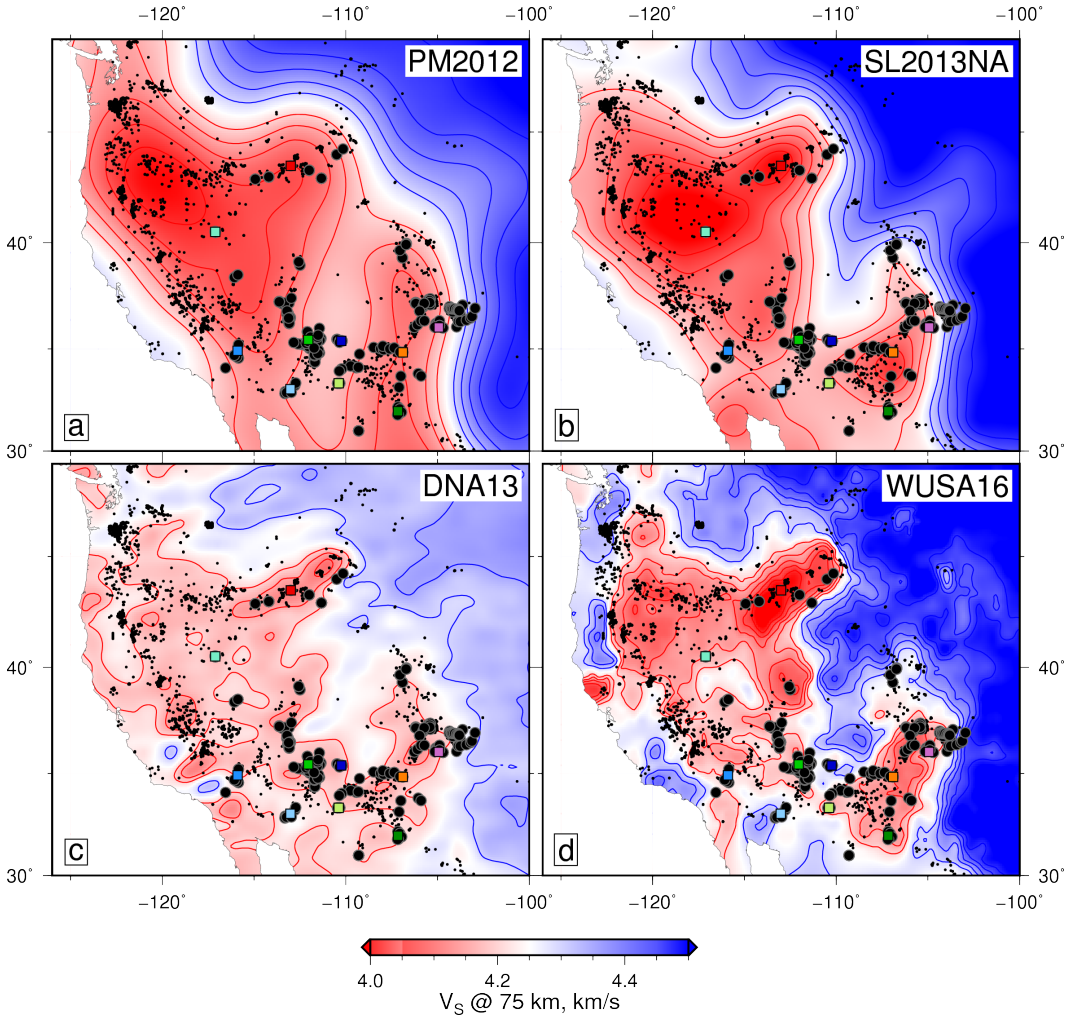
PM2012
SL2013NA
DNA13
WUSA16
a
b
c
d
−120°
−110°
−100°
40°
30°
4.0
4.2
4.4
V_S @ 75 km, km/s

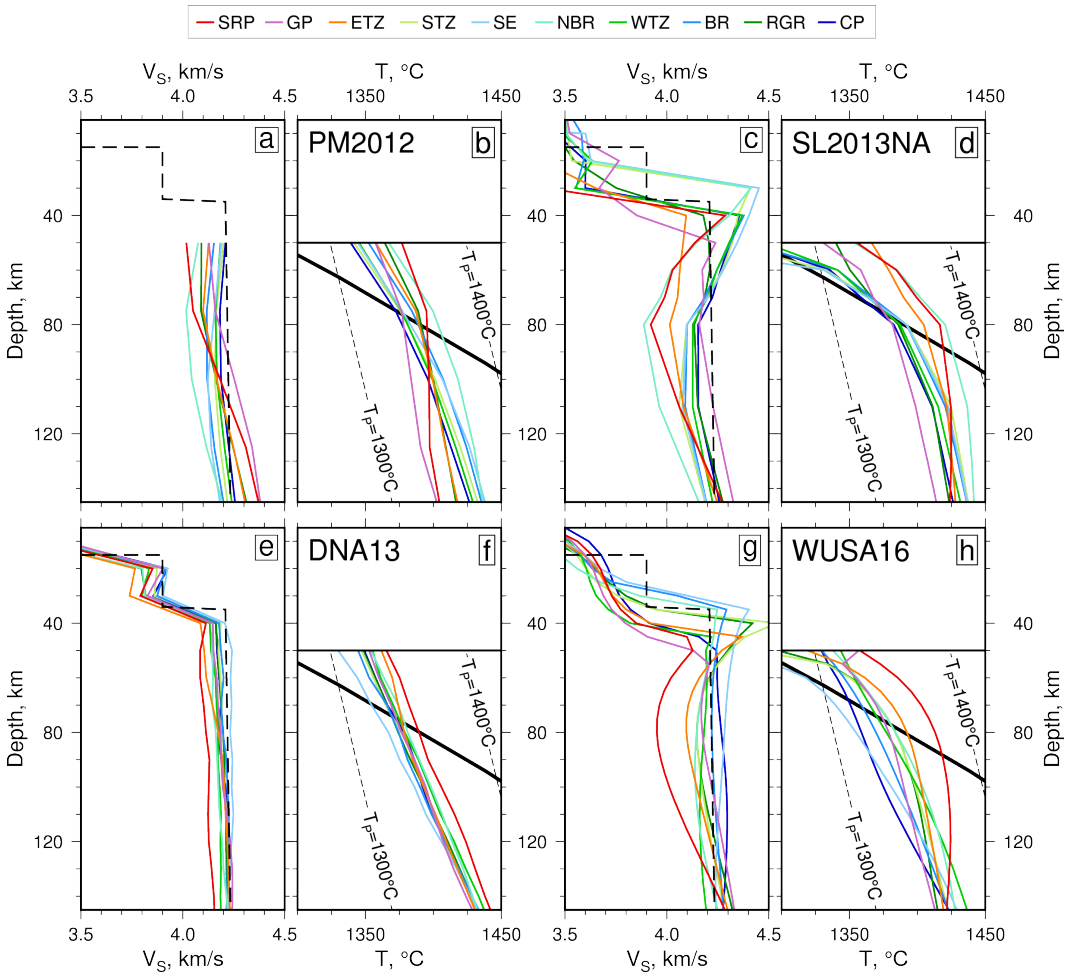
SRP
GP
ETZ
STZ
SE
NBR
WTZ
BR
RGR
CP
V_S, km/s
T, °C
Depth, km
a
PM2012
b
c
SL2013NA
d
e
DNA13
f
g
WUSA16
h
T_P=1400°C
T_P=1300°C

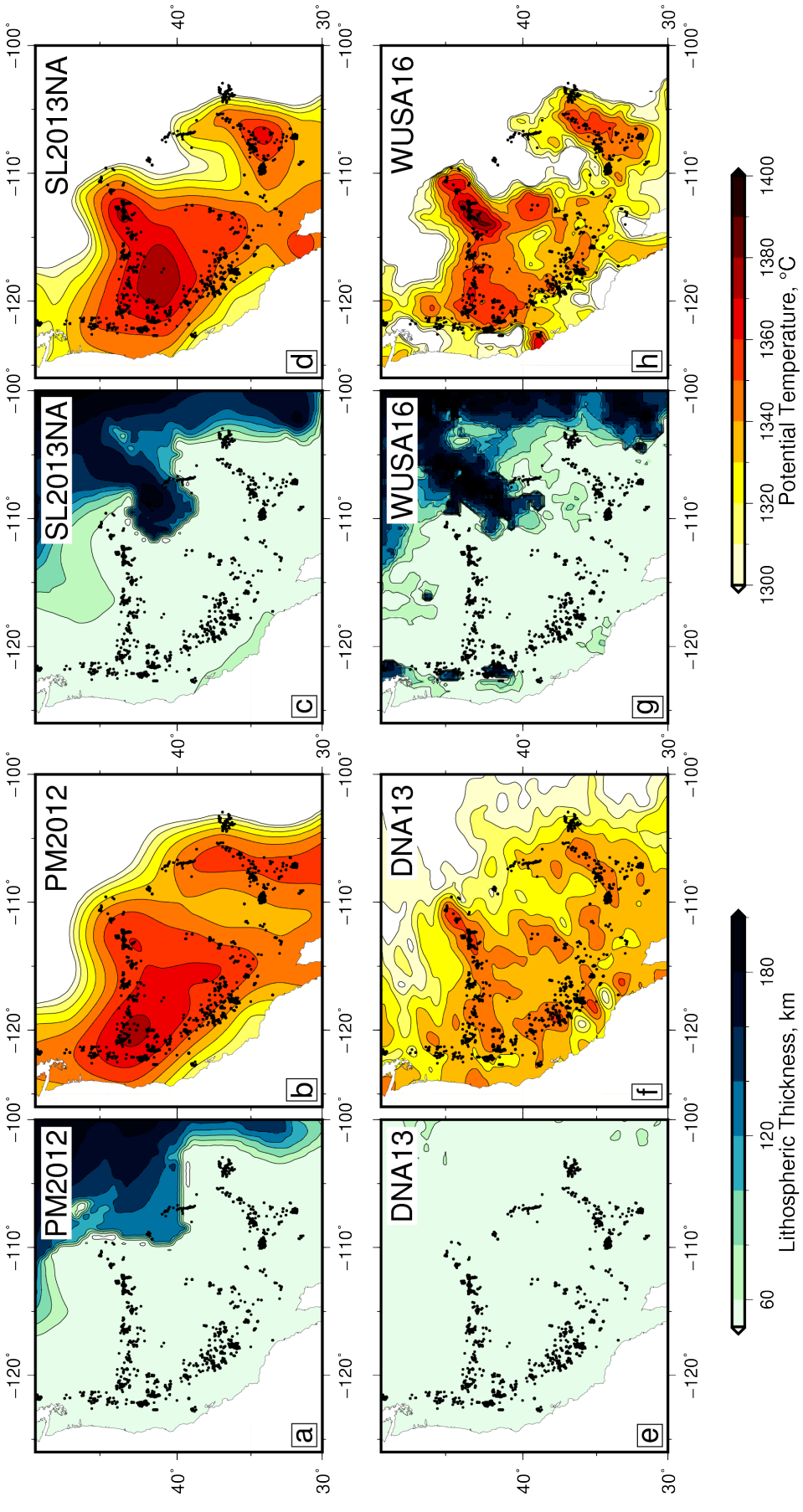
PM2012
SL2013NA
DNA13
WUSA16
a
b
c
d
e
f
g
h
−120°
−110°
−100°
40°
30°
60
120
180
Lithospheric Thickness, km
1300
1320
1340
1360
1380
1400
Potential Temperature, °C

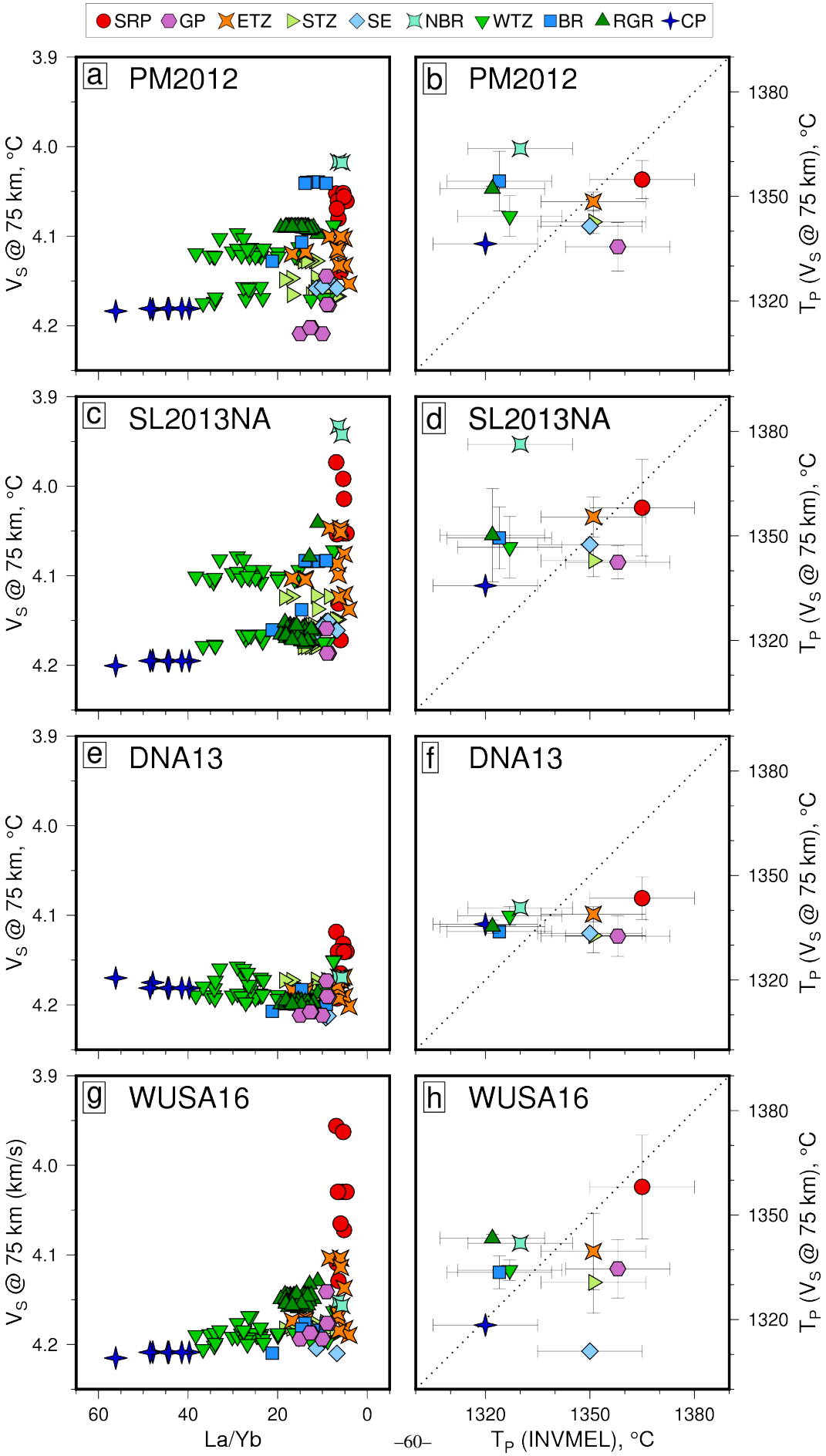
SRP GP ETZ STZ SE NBR WTZ BR RGR CP
a PM2012
b PM2012
c SL2013NA
d SL2013NA
e DNA13
f DNA13
g WUSA16
h WUSA16
V_S @ 75 km, °C
V_S @ 75 km (km/s)
T_P (V_S @ 75 km), °C
3.9
4.0
4.1
4.2
1380
1350
1320
60
40
20
0
La/Yb
T_P (INVMEL), °C

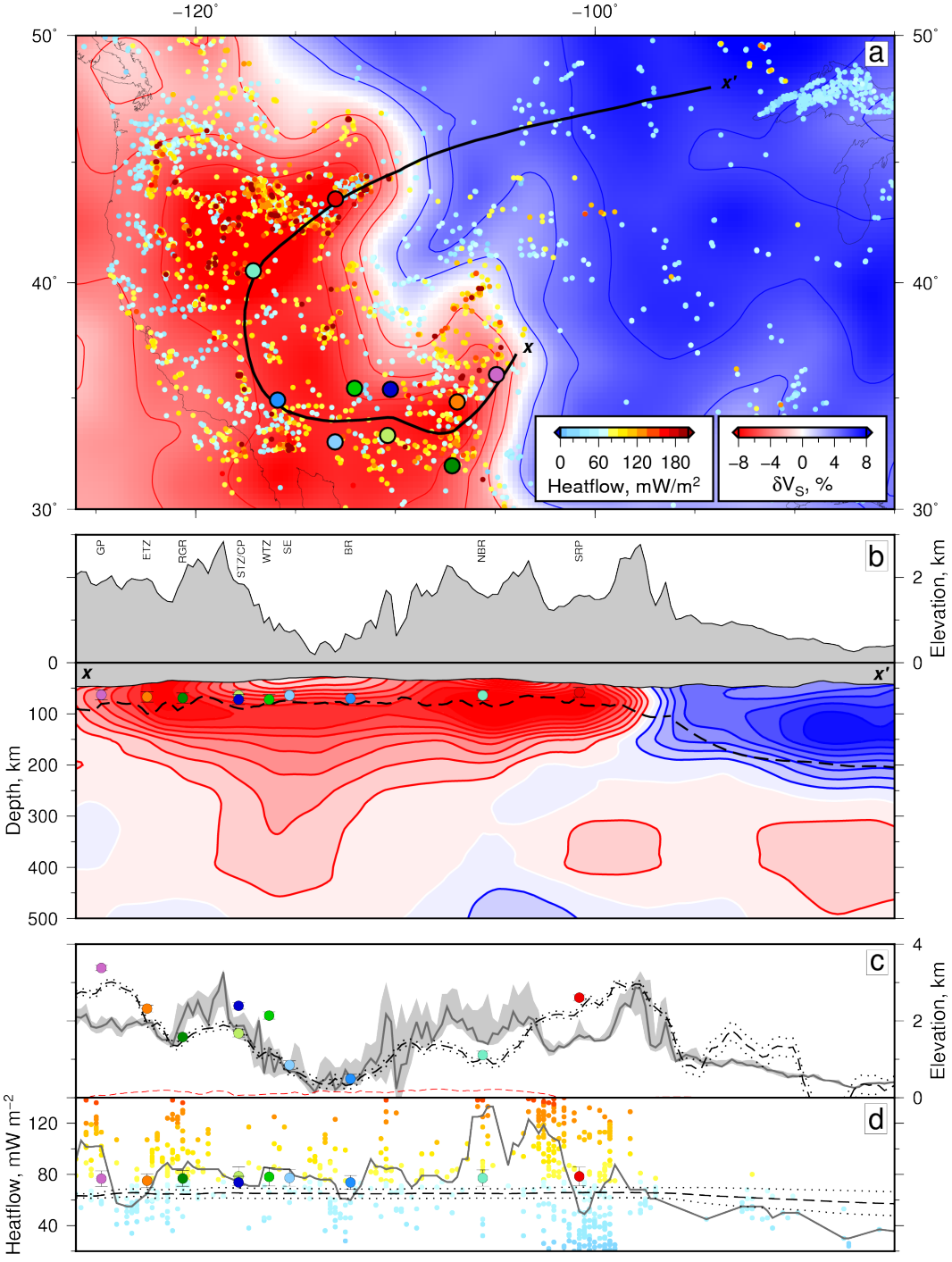
−120°
−100°
50°
40°
30°
a
x
x′
0 60 120 180
Heatflow, mW/m²
−8 −4 0 4 8
δVS, %
GP
ETZ
RGR
STZ/CP
WTZ
SE
BR
NBR
SRP
b
Elevation, km
Depth, km
100
200
300
400
500
c
d
Heatflow, mW m⁻²
120
80
40